EVALUATION OF STABILITY AND PERFORMANCE OF AN AIR-PROCESSED ALL-INORGANIC PEROVSKITE SOLAR CELL

by

Ruochen Shu

B.Eng., Donghua University, 2017

A THESIS SUBMITTED IN PARTIAL FULFILLMENT OF

THE REQUIREMENTS FOR THE DEGREE OF

MASTER OF APPLIED SCIENCE

in

THE FACULTY OF GRADUATE AND POSTDOCTORAL STUDIES

(Electrical and Computer Engineering)

THE UNIVERSITY OF BRITISH COLUMBIA

(Vancouver)

February 2022

© Ruochen Shu, 2022

The following individuals certify that they have read, and recommend to the Faculty of Graduate and Postdoctoral Studies for acceptance, the thesis entitled:

Evaluation of stability and performance of an air-processed all-inorganic perovskite solar cell

submitted by Ruochen Shu in partial fulfillment of the requirements for

the degree of Master of Applied Science

in Electrical and Computer Engineering

Examining Committee:

Dr. Peyman Servati, Professor, Department of Electrical and Computer Engineering, UBC
Supervisor

Dr. Alexander R. Uhl, Assistant Professor, School of Engineering, UBC
Supervisory Committee Member

Dr. Shahriar Mirabbasi, Professor, Department of Electrical and Computer Engineering, UBC
Supervisory Committee Member

Abstract

In the past decade, perovskite solar cells have attracted many concerns with the features of easy fabrication methods, high energy conversion efficiency, and relatively lower fabrication cost. Remarkable progress was witnessed on the power conversion efficiency from 3.8% to 25.5%, but the degradation issue is still one of the main barriers to the commercialization of perovskite solar cells.

Using the stable $CsPbBr_3$ as the photoactive material is regarded as a promising solution to improve device stability, however, degradation is also caused by other components in a device. The widely used Spiro-OMeTAD hole transporting material is expensive. It also needs the addition of p-dopants such as LiTFSI and 4-tBP to reach its peak performance. These additives exhibit poor stability against the harsh environment.

An inexpensive p-type semiconductor CuSCN can be an ideal alternative, owing to its chemical stability and unique electronic properties. In this work, the potential of dopant-free CuSCN acting as a stable hole transporting material for $CsPbBr_3$ solar cell was evaluated. High-quality $CsPbBr_3$ film was prepared through an optimized two-step solution method and incorporated into all-inorganic perovskite solar cells with low-temperature solution-processed CuSCN film. The entire fabrication process was completed in an ambient environment. The best device delivered a power conversion efficiency of 5.55%, with superior air stability, ultraviolet stability, and a wide operating temperature from -20 °C to 160 °C. However, a faster degradation was witnessed during long-term thermal aging. This work demonstrates that improved stability and suitable photovoltaic

performance can be achieved by using CuSCN as the hole transporting material of $CsPbBr_3$ perovskite solar cell, in comparison to other reported results in the literature.

Lay Summary

The stability of perovskite solar cells is one of the main factors affecting their commercialization, which can be enhanced through the use of stable raw materials. As the widely used organic semiconductors or organic-inorganic hybrid semiconductors present poor tolerance against the harsh environment, in this work, an all-inorganic perovskite solar cell was designed, fabricated, and optimized. A comprehensive evaluation of the stability and performance of the device was conducted, demonstrating that improved stability and suitable photovoltaic performance can be achieved by using inorganic semiconductors in perovskite solar cells. In addition, replacing expensive organic semiconductors with inexpensive inorganic semiconductors reduces the raw materials cost of perovskite solar cells as well. This work provides a pathway for the large-scale fabrication of efficient, stable, and inexpensive perovskite solar cells.

Preface

This research was done under the supervision of Dr. Peyman Servati in the Department of Electrical and Computer Engineering at the University of British Columbia.

Chapter 2 focuses on the fabrication and photovoltaic performance evaluation of all-inorganic perovskite solar cells. The author designed the project, conducted most of the experiments, and analyzed the data. Dr. Zenan Jiang in our group provided the preparation method of ZnO film. Ms. Anita Lam from the Department of Chemistry at UBC helped perform X-ray diffraction characterization.

Chapter 3 concentrates on the stability performance evaluation of all-inorganic perovskite solar cells fabricated in chapter 2. The author was responsible for the project design, experiment conduction, and data analysis.

Table of Contents

List of Tables

List of Figures

List of Abbreviations

CBM: Conduction band minimum

CIGS: Copper indium gallium selenide

EIS: Electrochemical impedance spectroscopy

ETL: Electron transporting layer

FF: Fill factor

HTL: Hole transporting layer

HOMO: Highest occupied molecular orbital

ITO: Indium-tin oxide

J_{sc}: Short-circuit current density

J–V: current density – voltage

LiTFSI: Lithium bis(trifluoromethanesulfonyl)imide salt

LUMO: lowest unoccupied molecular orbital

PCBM: Phenyl-C61-butyric acid methyl ester

PCE: Power conversion efficiency

PEDOT:PSS: Poly(3,4-ethylenedioxythiophene) polystyrene sulfonate

PSC: Perovskite solar cell

PTAA: Poly(triaryl)amine

P3HT: Poly (3-hexylthiophene)

RH: Room humidity

SEM: Scanning electron microscopic

Spiro-OMeTAD: 2,2′,7,7′-tetrakis(N,N-di-p-methoxyphenylamine)-9,9′-spirobifluorene

TCO: Transparent conductive oxide

UV: Ultra-violet

VBM: Valance band maximum

V_{oc}: Open-circuit voltage

XRD: X-ray diffractometer

4-tBP: 4-tert-Butylpyridine

Acknowledgements

Firstly and most importantly, I would like to express my deepest gratitude to my supervisor Dr. Peyman Servati, who provided insightful guidance and continuous support during my Master's study at UBC. Thank you for launching such a fantastic lab with the perfect equipment and excellent members, as well as encouraging me to explore and develop my research interests.

I would like to offer my sincere appreciation to my committee members Dr. Alexander R. Uhl and Dr. Shahriar Mirabbasi. Your comments and suggestions opened threads of thoughts that enriched my thesis.

I would like to extend my genuine thanks to Dr. Saeid Soltanian and Dr. Zenan Jiang, from whom I learned how to develop scientific ways of thinking. Thank you for your patience and suggestions to my endless questions on both academia and life, as well as equipment training in CFET and FEEL.

I would like to thank Dr. Fatemeh Zabihi for your useful feedback on my thesis writing, and Mr. Harun Arkaz and Ms. Siying Wu for selflessly sharing your experience that helped me solve the problems in experiments.

Thank you to Ms. Anita Lam who helped me perform X-ray diffraction, Dr. Mario Beaudoin who provided training on stylus profilometer in the cleanroom of AMPEL, and Ms. Heli Eunike who provided training on SEM in AMPEL.

Thank you to my colleagues at FEEL who are also my dearest friends, for your help, support, encouragement, and inspiration.

I would like to offer special thanks to my parents, who support my decision to move across the Pacific Ocean and study at UBC; and my hero Mr. Yuzuru Hanyu, who deeply inspires me when I chase my dream.

Dedication

To mom and dad

Chapter 1: Introduction

1.1 Needs statement of solar cells

From steam engines, lightbulbs to smart electronic products, people have been living with the benefits of electrical energy services for more than a century. The demand for energy dramatically increases with industrialization and population growth. However, due to the high dependence on high-carbon fossil fuels, serious environmental issues such as pollution and climate change have emerged globally. Fossil fuels are formed from the decomposition of organisms over millions of years. Limited supply, as well as following environmental issues, facilitate the development of renewable and clean alternatives. In 2019, hydro, biomass, and other renewables accounted for 13.7% of primary energy demand worldwide. Although fossil energy sources including oil, coal, and gas are still dominating the primary energy demand, a green energy revolution will reshape the layout of the global energy supply, and 21.4% of primary energy demand is forecast to come from renewables in 2045 (Figure 1.1) [1].

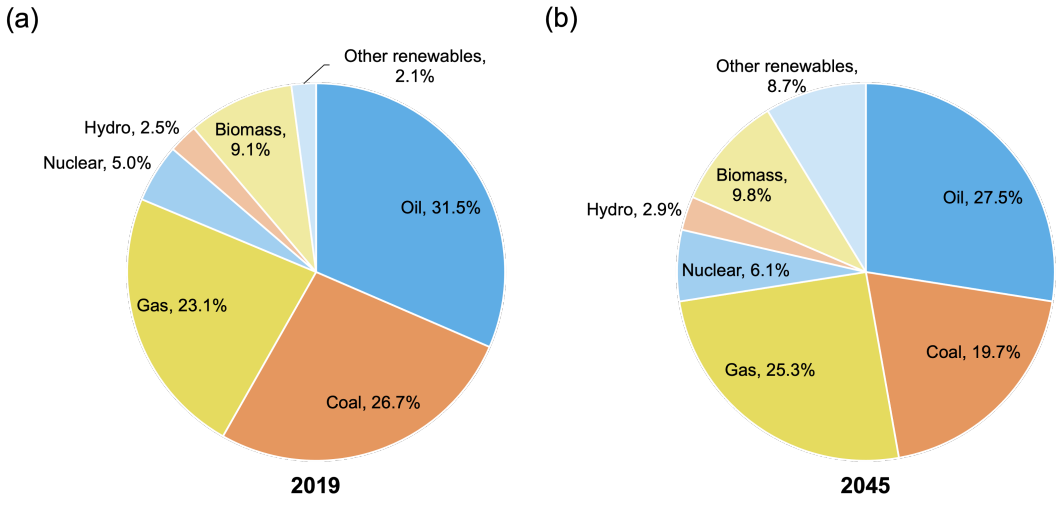

Figure 1.1 Distribution of primary energy demand worldwide in 2019 and 2045 [1]

Solar energy has become one of the most important renewable energy sources because of its abundance and flexibility. The earth receives 1.8×10^{14} kW of solar irradiation from the sun. Approximate 60% reaches the earth's surface while the rest is absorbed by the atmosphere or reflected back to space [2]. In the past ten years, global solar energy production increased from 21.03 to 694 TWh (Figure 1.2) [3].

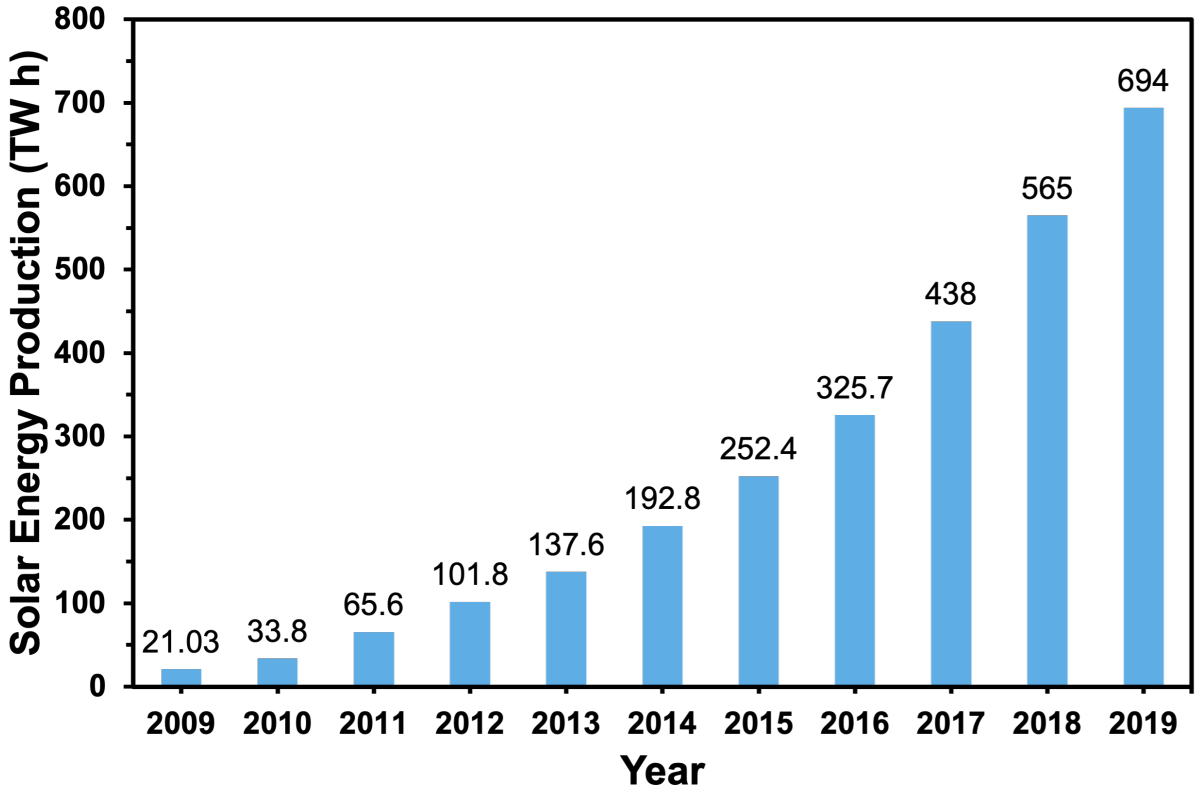

Figure 1.2 Solar energy production worldwide from 2009 to 2019 [3]

1.2 Classification of solar cells

A device that directly converts the energy of photons in light into electricity through the photovoltaic effect is called a solar cell. To balance cost and efficiency, huge efforts have been

exerted and revolutionary developments have been witnessed on solar cells over the past four decades, as shown in Figure 1.3 [4].

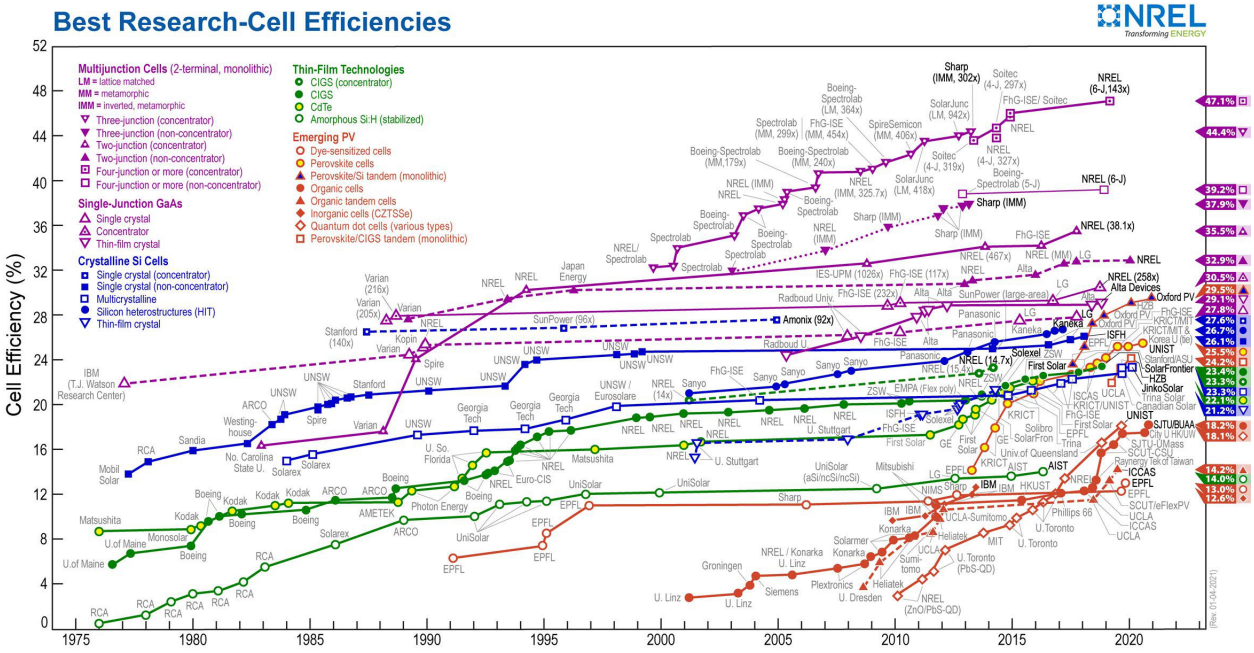

Figure 1.3 Best research-cell efficiency chart for various photovoltaic technologies plotted from 1976 to 2020 [4]

Since Silicon is the second most abundantly available element on earth, crystalline silicon solar cells became the earliest solar cells that are suitable for large-volume production [5], including polysilicon solar cells and monocrystalline silicon solar cells. Production cost was the biggest barrier in the early commercialization stage. Even till now, it is still on an unaffordable level compared with traditional energy resources.

More economic thin-film technology promoted the thin-film solar cells to be the second-generation solar cells. Thin-film solar cells include amorphous silicon (α-Si), CdTe, and CIGS solar cells. One of the most attractive features among the three materials is the direct bandgaps, which enable higher absorption rates of sunlight in the use of fewer materials. α-Si solar cells nearly extinguished in the market because of the low efficiency and the light-induced degradation. CdTe and CIGS solar cells have higher energy conversion efficiency, but the scarcity and toxicity of raw materials have limited their commercialization [6].

Plenty of research has been conducted on the third-generation advanced solar cells, primarily consisting of dye-sensitized solar cells, organic solar cells, quantum dot solar cells, and perovskite solar cells (PSCs). Among them, perovskite solar cells outshine with the features of easy fabrication methods, high energy conversion efficiency, and relatively low fabrication cost [7]. The first perovskite solar was developed in 2009 when Miyasaka *et al.* used perovskite crystal as the photoactive material for a dye-sensitized solar cell and obtained a power conversion efficiency (*PCE*) of 3.8% [8]. Within a short span of 10 years, remarkable progress was achieved and the efficiency was boosted up to 25.5% [4].

1.3 Stability of perovskite solar cells

A typical perovskite solar cell consists of a perovskite light-harvesting layer, charge transporting layers, and conductive electrodes. Figure 1.4 shows the device architecture of a conventional n-i-p and an inverted p-i-n planer perovskite solar cell. The transparent conductive oxide (TCO) and top electrode perform as the conductive electrodes, while the hole transporting layer (HTL) and the electron transporting layer (ETL) act as the interfaces for separating holes and electrons as well

as blocking opposite charges. The carriers are generated in the perovskite layer after light absorption and are transferred to the conductive electrodes through the transporting layers.

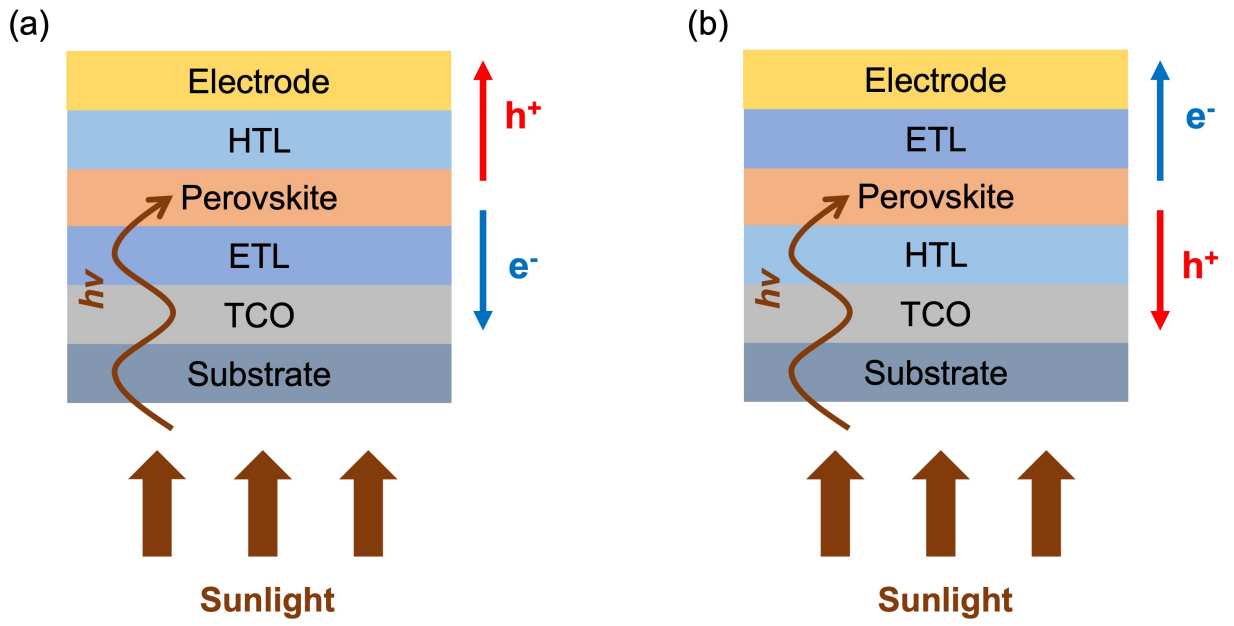

Figure 1.4 Device architecture of (a) conventional n-i-p and (b) inverted p-i-n planer perovskite solar cells

Despite the various advantages, the perovskite solar cells suffer from instability issues upon exposure to severe environments such as oxygen, moisture, high temperature, *etc.*, which is one of the key challenges of further commercialization. The sensitive perovskite materials and the other components of perovskite solar cells contribute to the degradation of devices upon direct contact with the external environment.

1.3.1 Perovskite layer

Similar to the mineral $CaTiO_3$, perovskites have a chemical formula ABX_3, in which A is a monovalent cation (*e.g.* $CH_3NH_3^+$, $CH_3CH_2NH_3^+$, $NH_2CH{=}NH_2^+$, Cs^+), B is a divalent metal cation (*e.g.* Pb^{2+}, Sn^{2+}, Ge^{2+}), and X is a monovalent halogen anion (*e.g.* I^-, Br^-, Cl^-) [9]. The ideal cubic structure of perovskite crystal is shown in Figure 1.5. The 6-fold coordinated B atom is surrounded by an octahedron consisting of X atoms, and the 12-fold coordinated A atom occupies the voids of the octahedral network.

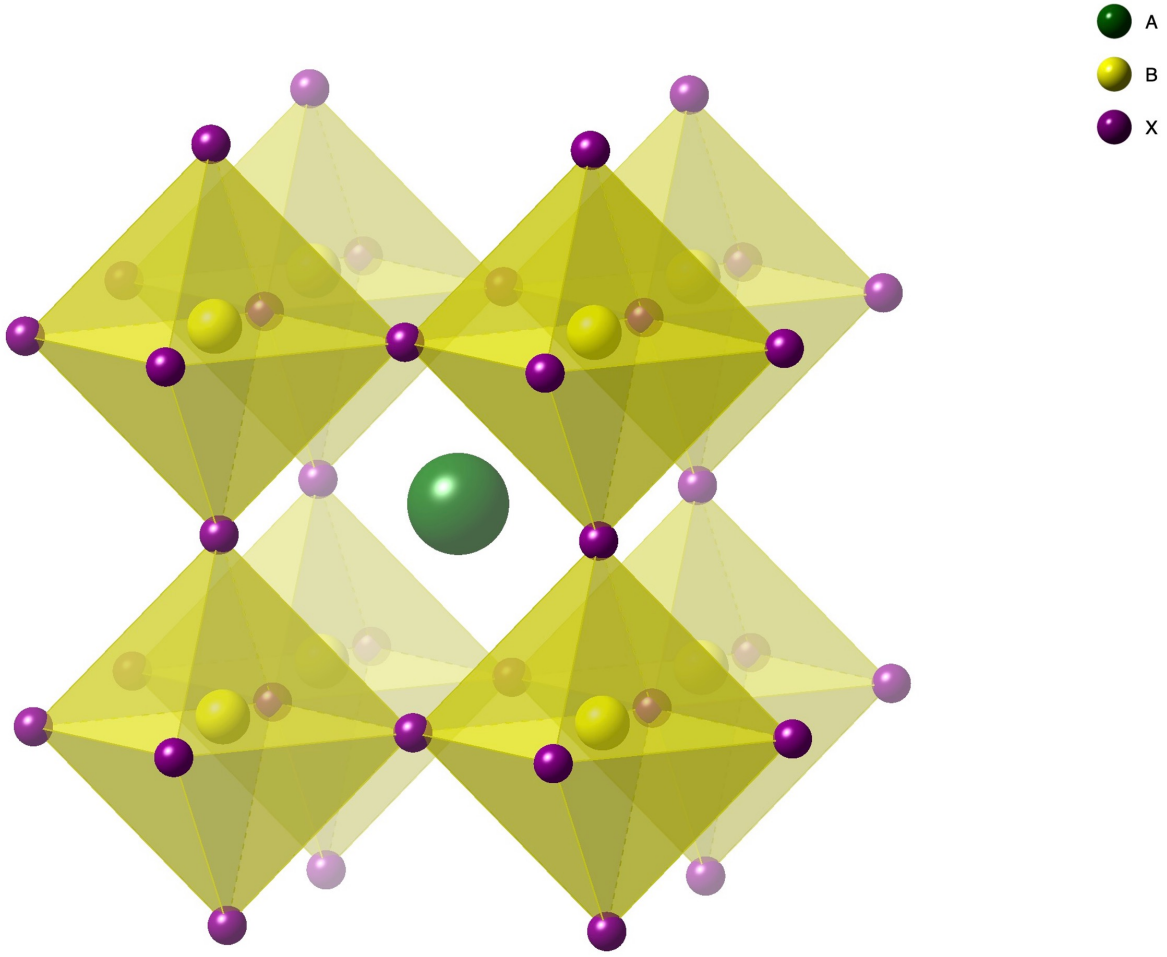

Figure 1.5 The extended network structure of perovskites

The phase stability of perovskite crystals can be determined by the Goldschmidt tolerance factor (t), which is calculated from the following formula:

$$t = \frac{r_A + r_X}{\sqrt{2}(r_B + r_X)}$$

Here, r_A, r_B, and r_X are the ionic radii of A, B, and X, respectively. To form the basic structure of perovskite, t should be maintained in the range of 0.81-1.11. When t is between 0.9 and 1.0, the crystal presents a stable cubic structure. Deviation of t causes the tilting of perovskite crystals, which may show orthorhombic, rhombohedral, hexagonal, or tetragonal structures [10].

Most studies of stability improvement focus on the modification of site A, as the changes have less sacrifice on the optoelectronic properties than modifying site B and X. Although $MAPbI_3$ has been widely used as a very efficient light harvester, the transition of tetragonal phase to cubic phase at 56 °C affects its bandgap and photovoltaic behavior [11]. Besides, the released protons from MA^+ under light form hydroiodic acid (HI) with I^- and cause the degradation of $MAPbI_3$ [12]. By replacing MA^+ with the larger FA^+, the tilt of the PbI_6 octahedra is changed and the t value increases from 0.91 to 0.99 [10]. The hydrogen bonding between FA^+ and PbI_6^- is stronger than that between MA^+ and PbI_6^-, leading to an improved photostability [12]. $FAPbI_3$ has been reported to be less vulnerable to high temperature compared with $MAPbI_3$, as no discoloration is observed in $FAPbI_3$ at 150 °C while $MAPbI_3$ discolors in 30 min [13]. However, undesirable phase transition of $FAPbI_3$ from the α-phase to non-perovskite δ-phase and the decomposition of FA^+ into ammonia occur upon exposure to humidity, which unfortunately makes $FAPbI_3$ degrade at a similar rate to $MAPbI_3$ [13–15].

Based on the instability issue of organic A cations, attention has been diverted to inorganic A cations. Li *et al*. enhanced the humidity stability of the *α*-phase by alloying $FAPbI_3$ with $CsPbI_3$. They found that the device with 15% Cs^+ ($FA_{0.85}Cs_{0.15}PbI_3$) had a more appropriate *t* value (0.95), which exhibited better photovoltaic performance and stability than the pristine $FAPbI_3$ device [16]. Slower degradation was observed in $FA_{0.9}Cs_{0.1}PbI_3$ film as well, both under a high humidity environment and continuous light soaking [17]. Triple cation (Cs/MA/FA) perovskite-based devices achieved a high *PCE* of 21.1% with good reproductivity. Only 10% loss was witnessed after full illumination for 250 h. A small fraction of Cs is effective in maintaining the perovskite in its *α*-phase, and the doping of MA induces defect-free crystal growth by reducing the crystallization rate [18]. Although adding Cs^+ improves the stability of organic perovskite, the purely inorganic perovskite $CsPbI_3$ has a low tolerance factor *t* of 0.81 resulting from the smaller ionic radius of Cs [19]. It forms the photoinactive orthorhombic *δ*-phase at room temperature, while the photoactive *α*-phase is only stable at 305-360 °C [20–22]. Wang *et al*. prepared the stable *α*-phase $CsPbI_3$ film using a solvent-controlled growth method. The $CsPbI_3$ solar cell achieved a lifetime of more than 500 h under continuously light soaking with a UV filter [23].

Site X modification has been pointed out to be an effective approach to further improve the device stability, by partially or completely replacing I with smaller Br or Cl. The smaller ionic radius of Br or Cl complements the smaller ionic radius of Cs, leading to a larger *t* value and more stable photoactive phases. Sanchez *et al.* found that, with Br fraction higher than 40%, the mixed halide $CsPbI_xBr_{(3-x)}$ inorganic perovskite solar cells maintained 90% of the original *PCE* after aging under full illumination for 1000 h or aging at 200 °C for 1 h [24]. $CsPbBr_3$ possesses orthorhombic *γ*-phase at room temperature, which converts to tetragonal *β*-phase and cubic *α*-phase at 88 °C and

130 °C, respectively [25]. Due to the ideal *t* value of 0.92, the three phases show similar properties [25], indicating outstanding air [26], moisture [27], thermal [27], and photochemical stability [28]. Most other reported perovskite solar cells need to be fabricated in nitrogen or inert atmosphere because of the rapid degradation of perovskites under ambient conditions. In contrast, $CsPbBr_3$ solar cells can be fabricated under ambient conditions, which reduces the cost of manufacture. Compared to $CsPbCl_3$ which has a large bandgap of 3.0 eV, the optical bandgap of $CsPbBr_3$ is 2.3 eV, which makes it more suitable for photovoltaic applications [25].

The B site also has an impact on the perovskite stability. For environmentally-friendly purposes, less toxic Sn and Ge have been studied as alternatives to the most widely used Pb. However, a decline in efficiency [29] and stability [30–31] have been reported. More efforts are required on developing efficient and stable Pb-free perovskite solar cells.

Compared with other organic and inorganic materials, $CsPbBr_3$ shows superiority on environmental tolerance with appropriate light-harvesting characteristics, revealing its potential as the photoactive layer for perovskite solar cells with high efficiency and stability. In the following parts, the role of charge transporting layers in device stability will be discussed, mainly in the case of $CsPbBr_3$-based perovskite solar cells.

1.3.2 Electron transporting layer

Efficient perovskite solar cells require electron transporting layers with high electron mobility and matched energy level. In the n-i-p perovskite solar cells (Figure 1.4 (a)), the electron transporting layer should present high light transmittance to reduce the loss of light. The features of the electron

transporting layer not only impact the photovoltaic performance of perovskite solar cells but are also linked with cell stability.

From dye-sensitized solar cells to perovskite solar cells, TiO_2 has been traditionally used as the electron transporting material. Li *et al.* deposited $CsPbBr_3$ film onto a compact TiO_2 layer by vapor deposition. The compact TiO_2 layer was prepared by spin-coating the titanium isopropoxide precursor solution and treating the substrate in a 40 mM aqueous solution of $TiCl_4$ at 70 °C [32]. Liang *et al.* added a layer of mesoporous TiO_2 on top of the compact TiO_2 [27], which can serve as a scaffold for perovskite nucleation and crystallization and facilitate electron extraction by increasing the interfacial contact area [33]. However, both compact TiO_2 and mesoporous TiO_2 layer fabrication requires high-temperature (> 450 °C) post-annealing treatment, introducing pinholes and cracks into the interface due to thermal stress [33]. In addition, the oxygen vacancies in TiO_2 adsorb oxygen in the air and desorb oxygen under UV irradiation, leading to degradation of the devices [34–35]. Although it is found that the presence of derivative $CsPb_2Br_5$ phase can passive the interface between TiO_2 and the perovskite layer and suppress the photocatalytic effect [32], the low electron mobility of TiO_2 (0.1–10 $cm^2\ V^{-1}\ s^{-1}$) limits the device performance [33].

SnO_2 and ZnO have been investigated as alternatives to TiO_2 because of their high electron mobility (100–200 $cm^2\ V^{-1}\ s^{-1}$ for SnO_2 and 200–300 $cm^2\ V^{-1}\ s^{-1}$ for ZnO) and low-temperature preparation feasibility [33]. Wang *et al.* and Zhao *et al.* used SnO_2 nanoparticles and quantum dots as electron transporting layers in $CsPbBr_3$ solar cells, respectively. The annealing temperature was less than 200 °C, and the devices showed excellent stability under continuous light soaking in 80% humidity or at 80 °C [23][36]. However, the quality of SnO_2 films was found to decrease after

high-temperature post-annealing, which requires the $CsPbBr_3$ film on top of it to be deposited at low temperature [37]. Zhang *et al.* and Chen *et al.* used ZnO materials as electron transporting layers in $CsPbBr_3$ solar cells, displaying strong tolerance to air and UV light [38–39].

In addition to inorganic materials, organic fullerene and its derivatives such as phenyl-C61-butyric acid methyl ester (PCBM) can also serve as the electron transporting material. With high electrical conductivity ($\sim 10^{-7}$ S cm^{-1}) and suitable energy level alignment, PCBM is normally used in inverted p-i-n perovskite solar cells [40], but not suitable for further industrialization because of its high cost and poor stability caused by photoinduced fullerene dimerization and thermal-induced dedimerization [41].

1.3.3 Hole transporting layer

With the function of hole extraction and electron blocking, the hole transporting layer plays an important role in device stability and performance. A milestone of perovskite solar cells is the substitute of the solid-state hole transporting material 2,2′,7,7′-tetrakis(N,N-di-p-methoxyphenylamine)-9,9′-spirobifluorene (Spiro-OMeTAD) for volatile liquid electrolyte, which delivers perovskite solar cells improved stability and efficiency. However, pristine Spiro-OMeTAD presents low conductivity and hole mobility (4×10^{-5} cm^2 V^{-1} s^{-1}), so p-dopants including lithium bis(trifluoromethanesulfonyl)imide (LiTFSI) and 4-tert-butylpyridine (4-tBP) are needed to oxidize Spiro-OMeTAD for enhancing the hole-conductivity [42]. Hygroscopic LiTFSI makes Spiro-OMeTAD vulnerable to moisture, and thermal-induced degradation is caused by the pyridination reaction of 4-tBP and oxidized Spiro-OMeTAD [43–44][45]. Light-induced charge recombination is also witnessed at the TiO_2/oxidized Spiro-OMeTAD interface [34][46].

PEDOT:PSS hole transporting material is generally used in inverted p-i-n perovskite solar cells, but the hygroscopicity of PEDOT:PSS limits the device stability as well [10]. Besides, the relatively low annealing temperature (< 200 °C) of the PEDOT:PSS hole transporting layer requires the upper $CsPbBr_3$ layer to be annealed at a lower low temperature, which is unfavorable for the crystallization of $CsPbBr_3$ film [41]. Poly(triaryl)amine (PTAA) and poly (3-hexylthiophene) (P3HT) with high carrier mobilities have been adopted as hole transporting material, and improved stability has been achieved [47–49]. However, like most organic hole transporting materials, their high cost is the main barrier to further commercialization.

The stronger intermolecular electron coupling that exists in inorganic hole conductors brings them intrinsic high stability and hole mobility, in comparison to the organic hole transporting materials. Inorganic p-type materials, such as CuPc, MnS, $Cu(Cr,M)O_2$, NiO_x have been studied as potential candidates for hole transporting layers. Although they delivered $CsPbBr_3$ solar cell enhanced air stability, moisture stability, or thermal stability, the relatively expensive deposition processes or complex synthesis methods are not suitable for large-scale production [50–53]. Besides, photo-induced degradation related to NiO_x was reported in other perovskite solar cells [54].

1.4 Thesis motivation

Perovskite materials have revolutionized the photovoltaic industry because of their superior photoelectric properties, such as high absorption coefficients, balanced carrier mobility, and suitable and adjustable energy bandgaps [10]. Despite the huge progress on device efficiency achieved in recent years, the stability of perovskite solar cells is one of the main challenges to their commercial-scale applications. The most studied organic-inorganic hybrid perovskite solar cells,

such as $MAPbI_3$ and $FAPbI_3$, are sensitive to light, oxygen, moisture, or heat. Therefore, a controlled environment (glovebox or dryroom) is needed during the fabrication process, and the cells suffer from dramatic degradation during long time exposure to the external environment.

With a bandgap of 2.3 eV and stable crystal structure, inorganic $CsPbBr_3$ perovskite material, which presents appropriate light-harvesting characteristics as well as outstanding stability under ambient environment, could be a game changer [25]. However, the device stability relies on not only the perovskite layer but also the other components in a device. The widely used organic hole transporting material Spiro-OMeTAD requires p-dopants including LiTFSI and 4-tBP for improving conductivity and hole mobility, but these additives have been found responsible for degradation [43–46]. Efforts should be made on finding stable, cheap, and easy-to-fabricate alternatives to expensive Spiro-OMeTAD.

Inorganic copper(I) thiocyanate (CuSCN) is a cheap and nontoxic intrinsic p-type semiconductor that has high stability, high hole mobility (10^{-1} cm^2 V^{-1} s^{-1}), and suitable energy level alignment with the perovskite [55]. CuSCN film can be easily prepared through a low-temperature solution processing technique [56]. These attractive photoelectrical properties as well as commercial availability make CuSCN an ideal candidate for replacing Spiro-OMeTAD hole transporting material.

To optimize the device stability of $CsPbBr_3$ solar cell, dopant-free p-type semiconductor CuSCN is studied in this project, as an alternative to expensive and unstable Spiro-OMeTAD hole transporting material. Compared to other reported devices in the literature, the CuSCN-based cell

exhibits suitable photovoltaic performance, outstanding air stability, UV stability, and wider operating temperature, while the thermal stability remains to be improved.

1.5 Thesis overview

The thesis contains four chapters. The present chapter introduced the background and degradation issue of perovskite solar cells. Previous research on improving the stability of perovskite solar cells was reviewed, in aspects of the perovskite layer, electron transporting layer, and hole transporting layer.

Chapter 2 presents the fabrication of air-processed all-inorganic perovskite solar cells. Optimization on the $CsPbBr_3$ layer as well as corresponding characterization results is discussed. A comparison is made across this work and previous literature based on the photovoltaic performance of the devices.

Chapter 3 evaluates the stability performance of the as-fabricated device from various aspects, including air stability, UV stability, temperature dependence, and thermal stability. Comparisons to results in previous literature are presented as well.

Chapter 4 provides a summary of the work and an outlook for future study.

Chapter 2: Fabrication and optimization of all-inorganic perovskite solar cell

2.1 Introduction

The performance of perovskite solar cells is influenced by various factors. In this chapter, the effect of energy-level alignment at the interfaces, thickness of each layer, and film quality of the perovskite layer on the photovoltaic properties of perovskite solar cells are discussed.

2.1.1 Energy level alignment

If a photon has energy equal to or greater than the bandgap of the material, the photon is absorbed and excites an electron to move from the valence band to the conduction band. An empty site is left in the valence band, which is called a "hole". To organic semiconductors, the valence band maximum (VBM) and the conduction band minimum (CBM) are roughly considered as the highest occupied molecular orbital (HOMO) and the lowest unoccupied molecular orbital (LUMO) level, respectively [57]. The generated electron and hole pairs are tightly bonded to each other. They must be dissociated against Coulomb force before they can be collected by the corresponding electrodes. Hence, the carrier transporting layers are introduced to achieve effective carrier separation. According to Koopmans' theorem, the negative of the energy of the HOMO (VBM to inorganic semiconductors) is equal to the first ionization energy of a molecule, while the negative of the energy of the LUMO (CBM to inorganic semiconductors) is equal to the electron affinity. Therefore, to enable smooth transfer and dissociation of the excited holes and electrons, the HOMO (VBM to inorganic semiconductors) of the hole transporting material must be higher than that of the photoactive material, while the LUMO (CBM to inorganic semiconductors) of the electron transporting material must be lower than that of the photoactive material, as illustrated in

Figure 2.2(a) in chapter 2.2.2. A well-aligned energy level is necessary for improving the photovoltaic performance of a solar cell. The electrical field facilitates the diffusion of carriers from the photoactive layer to the electrodes.

2.1.2 Thickness

The thickness of each layer is one of the major parameters in solar cell optimization. The Beer-Lambert law describes the relationship between absorbance and sample's concentration:

$$A = \varepsilon lc$$

where A, ε, l, and c are the absorbance, molar attenuation coefficient, length of the light path, and the concentration of the attenuating species, respectively. A thicker perovskite layer has more molecules that can interact with photons, increasing the absorbance and therefore generating more electron-hole pairs. However, the carrier recombination increases in a perovskite layer with an excessive thickness, due to the limitation of the carrier diffusion distance. Therefore, the *PCE* decreases after a certain point, even though the perovskite film absorbs more light energy [53]. The trend can be further explained by the following formula:

$$V_{oc} = (\frac{nKT}{q})\, ln(\frac{I_L}{I_0} + 1),$$

where n, k, T, q, I_L, and I_0 stand for the diode ideality factor, Boltzmann constant, temperature, elementary charge, photocurrent, and dark saturation current, respectively. Less carrier recombination occurs in a thinner photoactive layer, keeping a low I_0. V_{oc} increases with I_L, which is determined by the thickness of the photoactive layer. After reaching a certain thickness, I_0 increases and dominantly influences V_{oc}. V_{oc} starts to decline and reduce the *PCE* in turn [58].

Similar trends were observed in the electron transporting layer and hole transporting layer as well. A very thin electron transporting layer that cannot fully cover the ITO substrate would lead to the infiltration of the upper perovskite layer and insufficient blocking against the photo-generated holes, resulting in a decreased *PCE*. However, film transmittance decreases as film thickness increases, which has a negative effect on light absorption [59]. The thicker hole transporting layer increases the series resistance of the device but also decreases the possibility of short-circuiting in the device by preventing direct contact of the perovskite layer with the counter electrode [60]. Therefore, films with proper thickness are essential to achieve solar cells with a high *PCE*.

2.1.3 Perovskite film quality

As the core component of solar cells, the perovskite layer plays an important role in the device stability and performance. Several methods have been developed to prepare $CsPbBr_3$ film with good uniformity and high crystallinity, among which solution-processed methods are a simple and low-cost strategy. In the commonly used one-step solution method (Figure 2.1 (a)), CsBr and $PbBr_2$ with a molar ratio of 1:1 are dissolved into a suitable solvent, followed by the spin-coating process to remove the solvent and annealing process to facilitate perovskite crystallization. The commonly used solvents include dimethyl sulfoxide (DMSO), dimethylformamide (DMF), or a mixture. Unfortunately, the low solubility of CsBr in the above solvents limits the concentration of $CsPbBr_3$ precursor solution. Only a maximum concentration of 0.5 M can be achieved to maintain the 1:1 molar ratio of CsBr and $PbBr_2$, leading to thin and low-coverage $CsPbBr_3$ films [23][61–63].

To tackle the issue of the solubility difference between CsBr and $PbBr_2$, a two-step solution method has been developed. $PbBr_2$ solution is spin-coated onto the substrate in the first step. After the substrate annealing process, CsBr is introduced to react with the $PbBr_2$ film to form $CsPbBr_3$, by evaporation, dip coating, or spin coating [51][64–67].

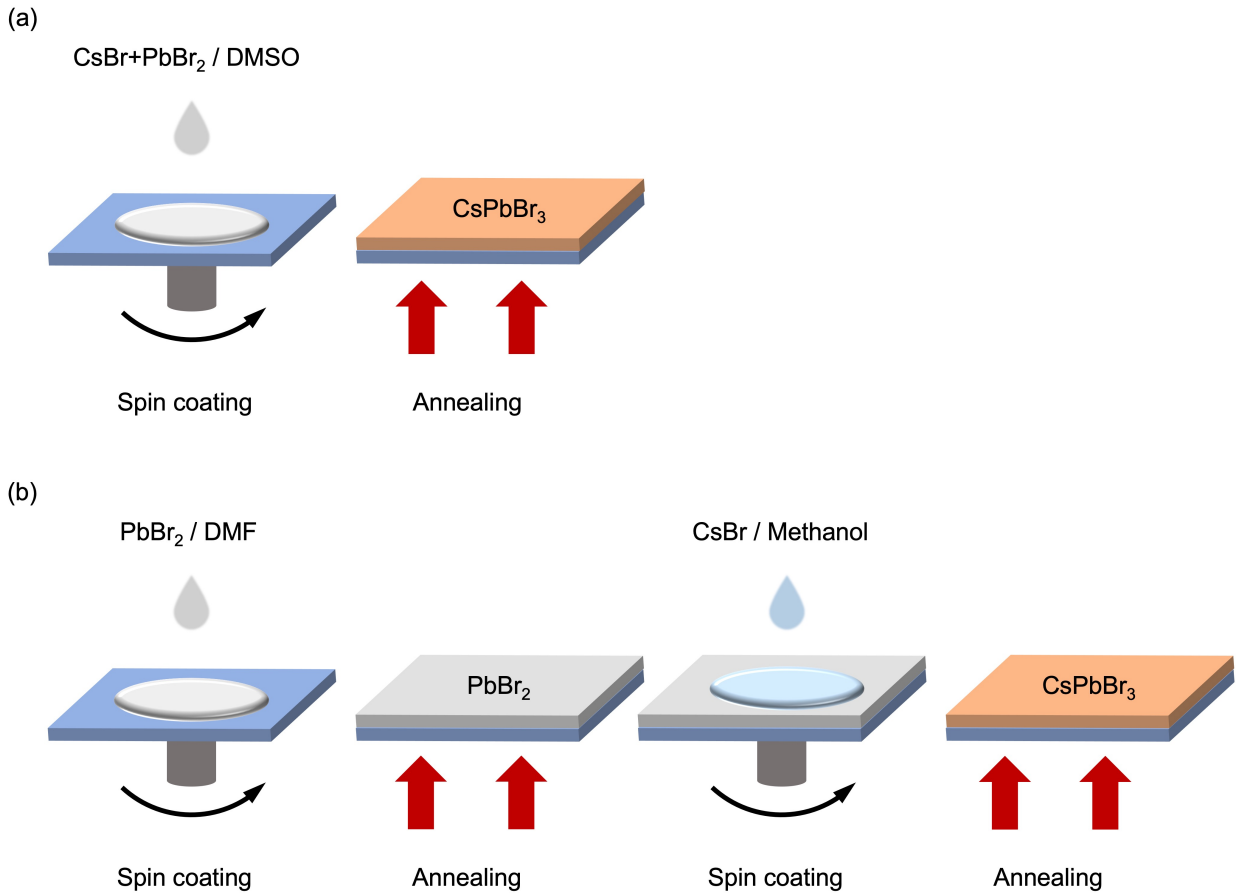

Figure 2.1 Schematic illustration of (a) one-step solution method and (b) two-step solution method to prepare $CsPbBr_3$ films

2.1.4 Chapter overview

In this chapter, $CsPbBr_3$-based all-inorganic perovskite solar cells are fabricated in an ambient environment, with low-temperature solution-processed CuSCN film acting as the hole transporting

layer. $CsPbBr_3$ films are prepared by the two-step solution method (Figure 2.1 (b)), and the phase purity is optimized by adjusting the number of CsBr deposition cycles. A comparison is made on photovoltaic performance between this work and the results in the literature.

2.2 Experimental section

2.2.1 Chemicals

Table 2.1 Information of the chemicals used in experiments

No.	Name	Assay	Supplier
1	Hydrochloric acid (HCl)	37%	Sigma-Aldrich
2	Nitric acid (HNO_3)	68–70%	Fisher Chemical
3	Zinc acetate dihydrate ($Zn(CH_3COO)_2 \cdot 2H_2O$)	≥98%	Sigma-Aldrich
4	2-Methoxyethanol ($CH_3OCH_2CH_2OH$)	≥99.0%	Sigma-Aldrich
5	Ethanolamine ($NH_2CH_2CH_2OH$)	≥98%	Sigma-Aldrich
6	Cesium bromide (CsBr)	99.999% trace metals basis	Sigma-Aldrich
7	Lead(II) bromide ($PbBr_2$)	99.999% trace metals basis	Sigma-Aldrich
8	*N,N*-Dimethylformamide ($HCON(CH_3)_2$)	≥99.8%	Fisher Chemical
9	Methanol (CH_3OH)	≥99.8%	Sigma-Aldrich
10	Copper(I) thiocyanate (CuSCN)	99%	Sigma-Aldrich
11	Diethyl sulfide ($(C_2H_5)_2S$)	98%	Sigma-Aldrich
12	Acetone ($(CH_3)_2CO$)	≥99.9%	Sigma-Aldrich
13	2-Propanol ($CH_3CHOHCH_3$)	≥99.5%	Sigma-Aldrich

2.2.2 Device fabrication

The planar solar cell devices with ITO/ZnO/$CsPbBr_3$/CuSCN/Au architecture were fabricated in an ambient environment. The energy level diagram and the device structure of the as-fabricated perovskite solar cell are shown in Figure 2.2 [68][51][69]. The thicknesses of ZnO film, CuSCN film, and gold electrode are 150 nm, 90 nm, and 120 nm, respectively.

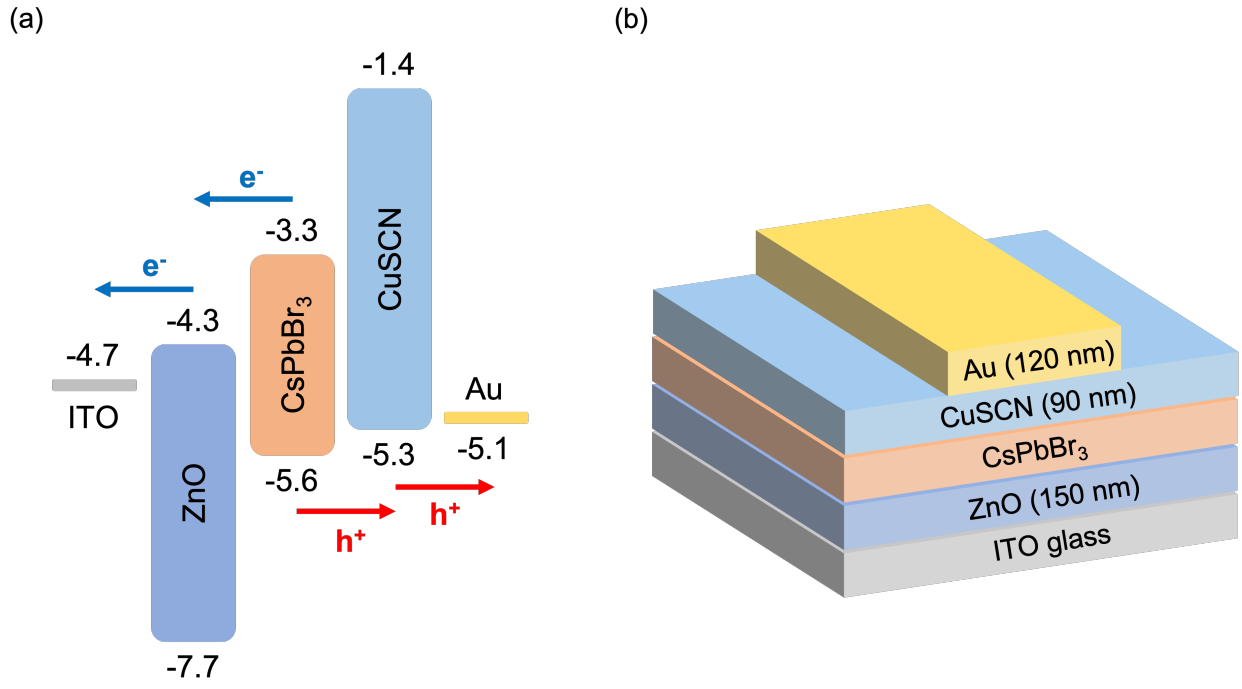

Figure 2.2 (a) Energy level diagram and (b) device structure of the as-fabricated perovskite solar cell

The glass substrate etching: ITO glass (2 cm × 2 cm) masked by Kapton tape was immersed into a mixture of HCl, HNO_3, and H_2O in a volume ratio of 4:1:5 at 50 °C for 15 min. After rinsing with DI water, the Kapton tape was removed from the glass.

The glass substrate cleaning: The etched ITO glass was cleaned with detergent, DI water, acetone, and isopropyl alcohol in an ultrasonic cleaner for 10 min, respectively. After being dried under nitrogen gas flow, the glass was treated with oxygen plasma for 3 min before using, to remove the organic residue as well as improve the surface energy and wettability of ITO.

The electron transporting layer deposition [68]: 2.1951 g zinc acetate dihydrate and 610.8 μL ethanolamine were dissolved in 10 mL 2-methoxyethanol at 60 °C under vigorous stirring for 30 min. The as-prepared ZnO precursor ink was deposited on the ITO substrate by spin coating at 3000 rpm for 10 s, followed by annealing at 250 °C for 5 min. This process was repeated three times.

The photoactive layer deposition was adapted from ref. [67]: $PbBr_2$ was dissolved in DMF at 80 °C under vigorous stirring overnight to prepare 1 M solution. The ZnO-coated substrate was pre-heated at 90 °C for 5 min before spin-coating. The as-prepared solution was spin-coated onto ZnO film at 2000 rpm for 30 s and then annealed at 90 °C for 1 h. The substrate was covered by a petri dish during the annealing process. CsBr was dissolved in methanol at 50 °C under vigorous stirring for 1 h to prepare 0.07 M solution. The solution was spin-coated onto $PbBr_2$ film at 2000 rpm for 30 s and then annealed at 250 °C for 5 min. This process was repeated several times to optimize the phase purity of perovskite layers. The explanations of sample labels that appear in this chapter and the thicknesses of $CsPbBr_3$ films are listed in Table 2.2.

Table 2.2 Explanations of sample labels and thicknesses of $CsPbBr_3$ films

Sample label	Explanation	Film thickness (nm)
CsBr-5	$CsPbBr_3$ film prepared from 5-cycle CsBr deposition or corresponding PSC	430
CsBr-6	$CsPbBr_3$ film prepared from 6-cycle CsBr deposition or corresponding PSC	490
CsBr-7	$CsPbBr_3$ film prepared from 7-cycle CsBr deposition or corresponding PSC	550
CsBr-8	$CsPbBr_3$ film prepared from 8-cycle CsBr deposition or corresponding PSC	605

The hole transporting layer deposition was adapted from ref. [70]: 35 mg CuSCN was dissolved in 1 mL diethyl sulfide at room temperature under vigorous stirring overnight. The solution was filtered by a 0.45 μm PTFE syringe filter before use. 100 μL solution was spin-coated onto the perovskite film at 3000 rpm for 30 s and then annealed at 60 °C for 10 min.

The gold electrode deposition: 120 nm gold layer was deposited onto the substrate by plasma sputter coater. The substrate was covered by a mask during the sputtering process to obtain patterned coating. The active area of each cell was 2 mm × 5 mm.

2.2.3 Characterization

The composition and crystal orientation of $CsPbBr_3$ was recorded by the Bruker D8-Advance X-ray diffractometer. The UV-visible absorption spectra were characterized by the Cary 7000 Universal Measurement Spectrophotometer. The scanning electron microscopic (SEM) images

were obtained by the ZEISS Sigma Field Emission SEM. The film thickness was measured by the Bruker XT Dektak profilometer. The current density – voltage (J–V) curves were measured through the Keithley 2400 source meter under AM 1.5G illumination (100 mW cm^{-2}) provided by a solar simulator (Newport Co.). The electrochemical impedance spectroscopy (EIS) data was obtained by the BioLogic VMP300 electrochemical workstation.

2.3 Results and discussion

2.3.1 Crystallinity and purity study of the perovskite

$PbBr_2$ film appeared white, but after being covered by CsBr solution multiple times, the film turned yellow gradually. To study the formation mechanism of perovskite film, the films prepared from different CsBr spin-coating cycles were characterized through XRD. As shown in Figure 2.3, phase conversion occurs during this process, and can be depicted into the following three reactions:

$$2PbBr_2 + CsBr \rightarrow CsPb_2Br_5$$

$$CsPb_2Br_5 + CsBr \rightarrow 2CsPbBr_3$$

$$CsPbBr_3 + 3CsBr \rightarrow Cs_4PbBr_6$$

The phase purity of $CsPbBr_3$ is one of the most determinant factors. $CsPb_2Br_5$ is reported to exhibit a large indirect bandgap of 3.0–3.1 eV and a photoluminescence-inactive behavior [71–72], and Cs_4PbBr_6 is reported to exhibit low photocurrent generation [73], which are detrimental to the photovoltaic performance of a device and expected to be eliminated.

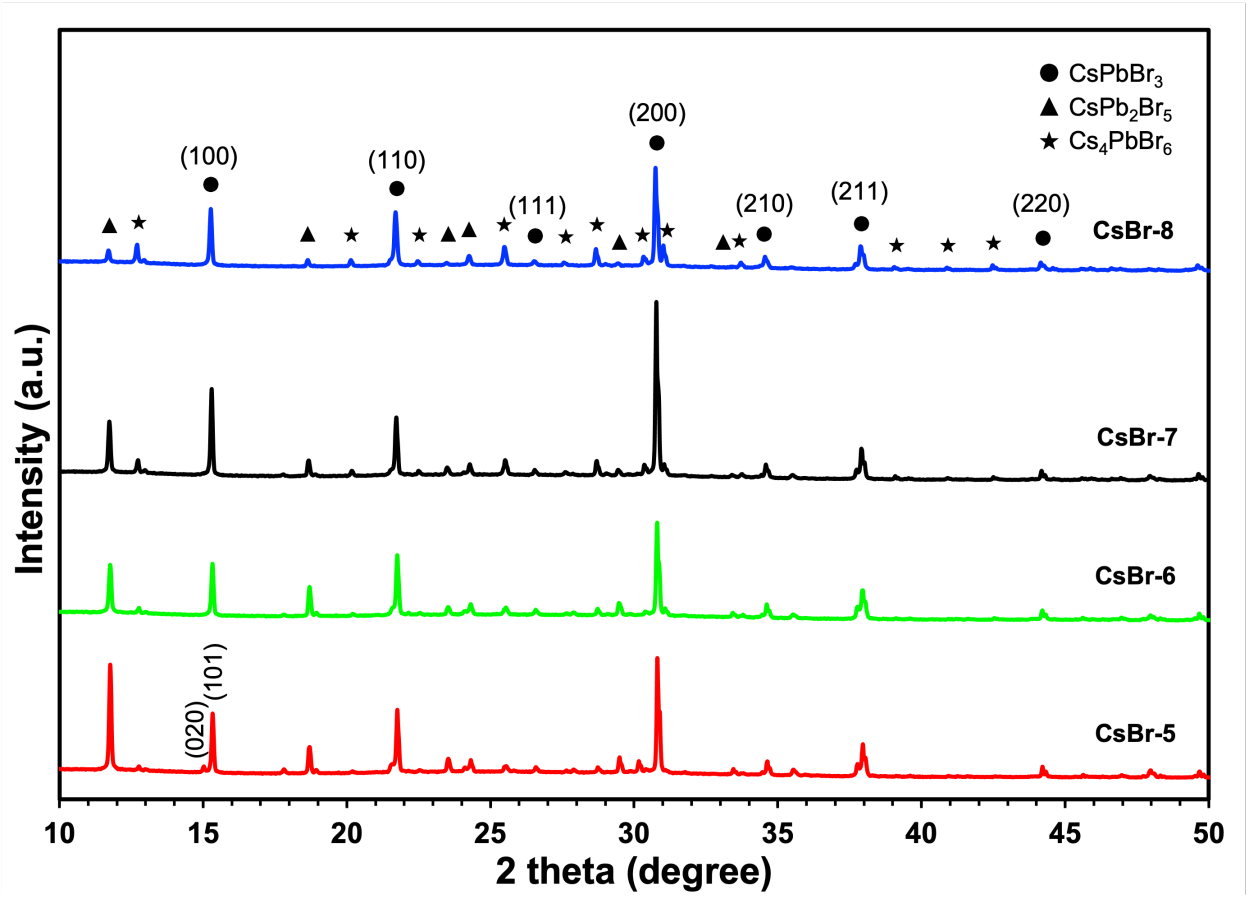

Figure 2.3 XRD spectra of $CsPbBr_3$ samples prepared from different CsBr deposition cycles

All samples exhibit $CsPbBr_3$ diffraction peaks at 15.2°, 21.7°, 26.5°, 30.8°, 34.4°, 37.9°, and 44.1°, corresponding to the (100), (110), (111), (200), (210), (211), and (220) planes of the cubic $CsPbBr_3$ phase, respectively [74–76]. At n =5, a splitting of the diffraction peak appears at 15.2°, matching the (020) and (101) planes of the orthorhombic $CsPbBr_3$ phase [62]. The orthorhombic phase disappears when further increasing the number of CsBr deposition cycles. At n = 5 and 6, significant $CsPb_2Br_5$ phases can be observed, resulting from excessive $PbBr_2$ in the system. With CsBr spin-coating cycle increases, $PbBr_2$ becomes less dominant, and CsBr reacts with $CsPb_2Br_5$ to form $CsPbBr_3$. At n = 7, the $CsPbBr_3$ diffraction peak at 30.8° is the strongest compared with

other samples, indicating the optimization of $CsPbBr_3$ grain crystallinity. Further increasing the spin-coating cycle introduces an excess amount of CsBr into the system, leading to a conversion of $CsPbBr_3$ to Cs_4PbBr_6. It is noticed that the $CsPb_2Br_5$ phase cannot be fully consumed during the whole fabrication process, even at a CsBr-rich phase system. This comes from the fact that $CsPbBr_3$ can convert to the tetragonal $CsPb_2Br_5$ phase at 200–300 °C [77].

2.3.2 Optical properties

The absorption ability of $CsPbBr_3$ film is of critical importance to the photovoltaic performance of perovskite solar cells. $CsPbBr_3$ films with stronger absorption can absorb more optical photons and generate more carriers, therefore leading to higher I_{sc}. To identify the absorption ability of $CsPbBr_3$ films prepared from different CsBr deposition cycles, the UV-visible spectrum was used for characterization.

A molecule absorbs light when the energy of the incoming light is equal to or larger than the energy difference between the excited state and the ground state of the molecule. The Planck equation describes the relationship between the wavelength and the energy of light:

$$E = h\frac{c}{\lambda}$$

where E is the energy of light, h is the Planck constant, c is the speed of light, and λ is the wavelength of light. According to the Planck equation, strong absorption often occurs at the ultraviolet region with the wavelength from 200 nm to 400 nm, while long-wavelength near-infrared light does not have sufficient energy and therefore is poorly absorbed. The absorbance can be measured by a UV-visible spectrophotometer based on the following equation:

$$A = -log\frac{I}{I_0} = -log\frac{\%T}{100\%}$$

where A is the absorbance, I_0 is the initial intensity of light, I is the intensity of light after passing through the sample, and $\%T$ is the transmittance. The UV-vis absorption spectrum of a sample exhibits the absorbance values at different wavelengths.

A bandgap of a semiconductor describes the minimum amount of energy needed for an electron in the semiconductor to be excited from the valence band to the conduction band and can be calculated by Tauc plot analysis. The Tauc plot is based on the equation:

$$(\alpha h\nu)^{\frac{1}{\gamma}} = A(h\nu - E_g)$$

where α is the absorption coefficient of the sample, h is the Planck constant ($h = 6.63 \times 10^{-34} J\ s = \frac{6.63\times10^{-34}}{1.6\times10^{-19}} eV\ s$), ν is the photon's electromagnetic frequency ($\nu = \frac{c}{\lambda} = \frac{3\times10^{8}\ m\ s^{-1}}{\lambda}$), A is a constant, E_g is the bandgap energy, and γ factor has a value equal to $\frac{1}{2}$ or 2 for allowed direct transition or allowed indirect transition, respectively [78]. $CsPbBr_3$, ZnO, and CuSCN are all direct bandgap semiconductors, of which the VBM and CBM occur at the same value of crystal momentum. A Tauc plot shows the $(\alpha h\nu)^2$ versus $h\nu$. Extrapolate the linear region to the X-axis. The value of the point where the line intersects the X-axis is the band gap value.

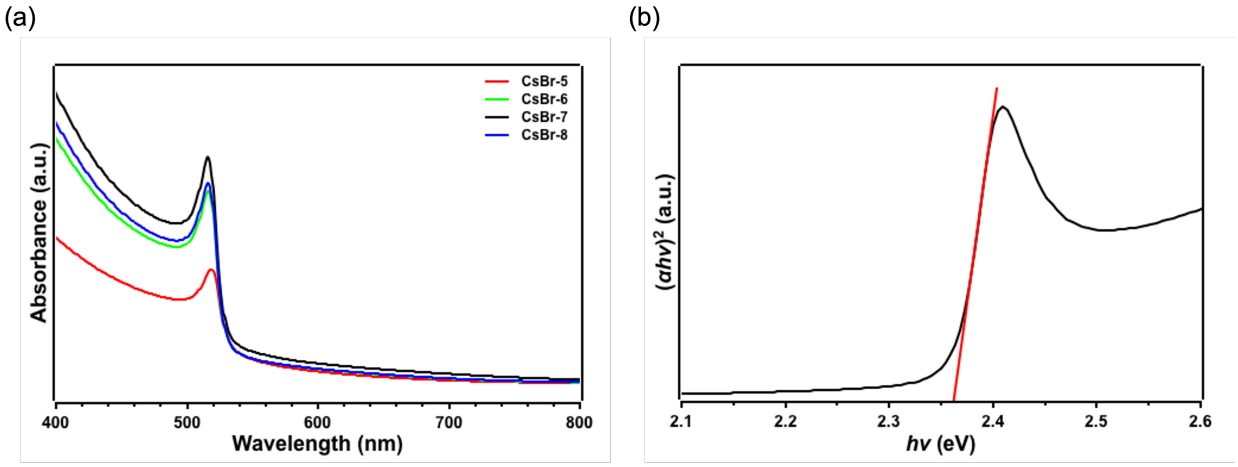

Figure 2.4 (a) UV-vis absorption spectra of $CsPbBr_3$ samples prepared from different CsBr deposition cycles and (b) Tauc plot of the CsBr-7 sample

As shown in Figure 2.4 (a), with increasing CsBr deposition cycles, the absorbance of $CsPbBr_3$ film first increases and then decreases. The highest absorbance occurs in the CsBr-7 sample, which is the sample with the highest crystallinity in XRD results. All samples show an absorption spectrum edge at ~540 nm, and an exciton-induced absorption peak at ~520 nm. Tauc plot analysis (Figure 2.4 (b)) suggests that the CsBr-7 sample processes an optical bandgap of 2.36 eV.

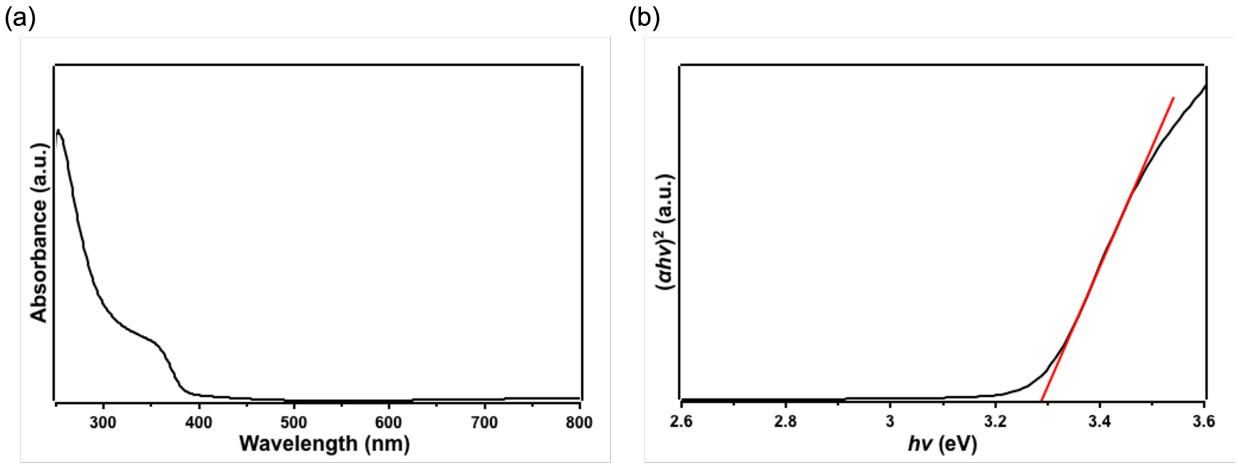

Figure 2.5 (a) UV-vis absorption spectrum and (b) Tauc plot of ZnO film

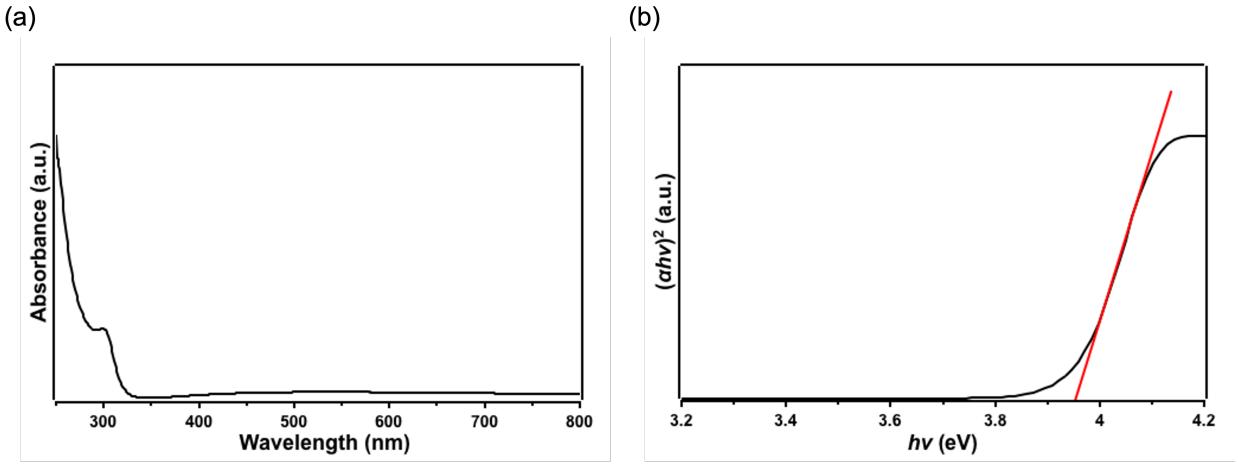

Figure 2.6 (a) UV-vis absorption spectrum and (b) Tauc plot of CuSCN film

Light passes through the electron transporting layer before being absorbed by the photoactive layer, which requires an electron transporting layer with high light transmittance to reduce the loss of light. Using blocking materials with suitable bandgaps guarantees the high performance of a solar cell. Therefore, similar tests were conducted on ZnO and CuSCN films as well, of which the absorbance was studied and optimized. As shown in Figure 2.5 (a), ZnO film presents poor

absorbance at wavelengths above 400 nm that represents high transmittance (> 90%) in turn. The optical bandgap of ZnO and CuSCN films are 3.28 eV (Figure 2.5 (b)) and 3.95 eV (Figure 2.6 (b)), respectively, which are consistent with the values reported in previous research [79–80]. A summary of the optical band gap value of each layer is given in Table 2.3.

Table 2.3 Summary of the optical bandgap value of each layer

Layer	The optical band gap (eV)
ZnO	3.28
$CsPbBr_3$	2.36
CuSCN	3.95

2.3.3 Morphology and thickness study

The performance of a perovskite solar cell highly depends on the film quality. Due to the formation of shunting pathways and even short circuits, pinholes and cracks in films can cause voltage loss. Therefore, full-coverage films are expected to deliver high V_{oc}.

The morphology of each layer was characterized with SEM. As shown in Figure 2.7 (a) and Figure 2.7 (b), both ZnO film and CuSCN film demonstrates full coverage. The grain size of ZnO film and CuSCN film is ~20 nm and ~40 nm, respectively. Normally, a large grain size of photoactive film leads to decreased grain boundary density and trap states density. Energy loss is reduced and charge recombination is suppressed, which enhances the photovoltaic performance of the devices [81]. Figure 2.7 (c) and (d) present the top-view SEM images of $PbBr_2$ and $CsPbBr_3$ films,

respectively. Pinholes and relatively smaller grains can be observed in $PbBr_2$ film. After 7-cycle CsBr deposition, full-coverage $CsPbBr_3$ film is formed, with a larger grain size of ~1 μm.

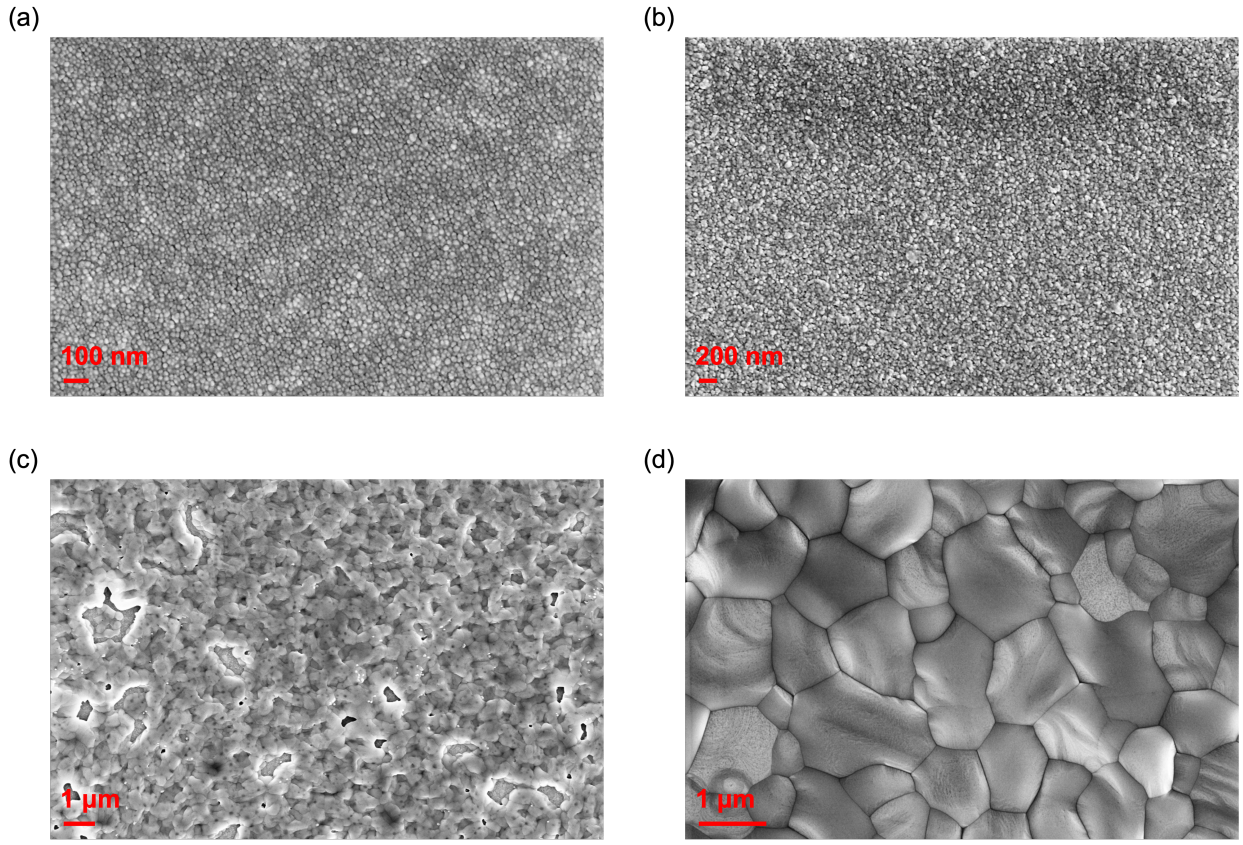

Figure 2.7 SEM images of (a) ZnO, (b) CuSCN, (c) $PbBr_2$, and (d) $CsPbBr_3$ films

Fabricating a highly efficient solar cell requires films with proper thickness. Thin blocking layers cause insufficient blocking of carriers, while thick blocking layers increase the series resistance and reduce the light loss because of decreased film transmittance. The thicknesses of ZnO and CuSCN films are 150 nm and 90 nm, respectively. A thin perovskite layer generates low photocurrent, while a thick perovskite layer increases the series resistance and the carrier recombination rate due to the limitation of carrier diffusion lengths. CsBr-7 sample exhibits the

strongest absorption ability, of which the thickness is 550 nm. The thicknesses of CsBr-5, CsBr-6, and CsBr-8 samples are 430 nm, 490 nm, and 605 nm, respectively.

The pinhole-free films were applied to the later devices for optimal device performance.

2.3.4 Photovoltaic properties

The basic photovoltaic parameters of a solar cell are determined by the current (I) – voltage (V) curve. The short-circuit current I_{sc} is the current through the solar cell when there is no voltage drop across the cell, which is usually listed in the form of short-circuit current density J_{sc} to eliminate the dependence of solar cell area. I_{sc} is the maximum current a solar cell can produce. The open-circuit voltage V_{oc} occurs when no current flows in the solar cell, representing the largest voltage that can be obtained from the solar cell. The solar cell outputs maximum power P_{max} at a point between short-circuit status and open-circuit status, which is the ideal operating condition of the cell. Therefore, the power conversion efficiency *PCE* is defined by the following formula:

$$PCE = \frac{P_{max}}{P_{in}} \times 100\%$$

where P_{max} is the maximum output power of the cell and P_{in} is the input power from the sun. Fill factor (*FF*) is another measure of the solar cell quality, defined by the following formula:

$$FF = \frac{P_{max}}{V_{oc} \times I_{sc}} \times 100\%$$

where P_{max}, V_{oc}, and I_{sc} stand for the maximum output power, open-circuit voltage, and short-circuit current, respectively.

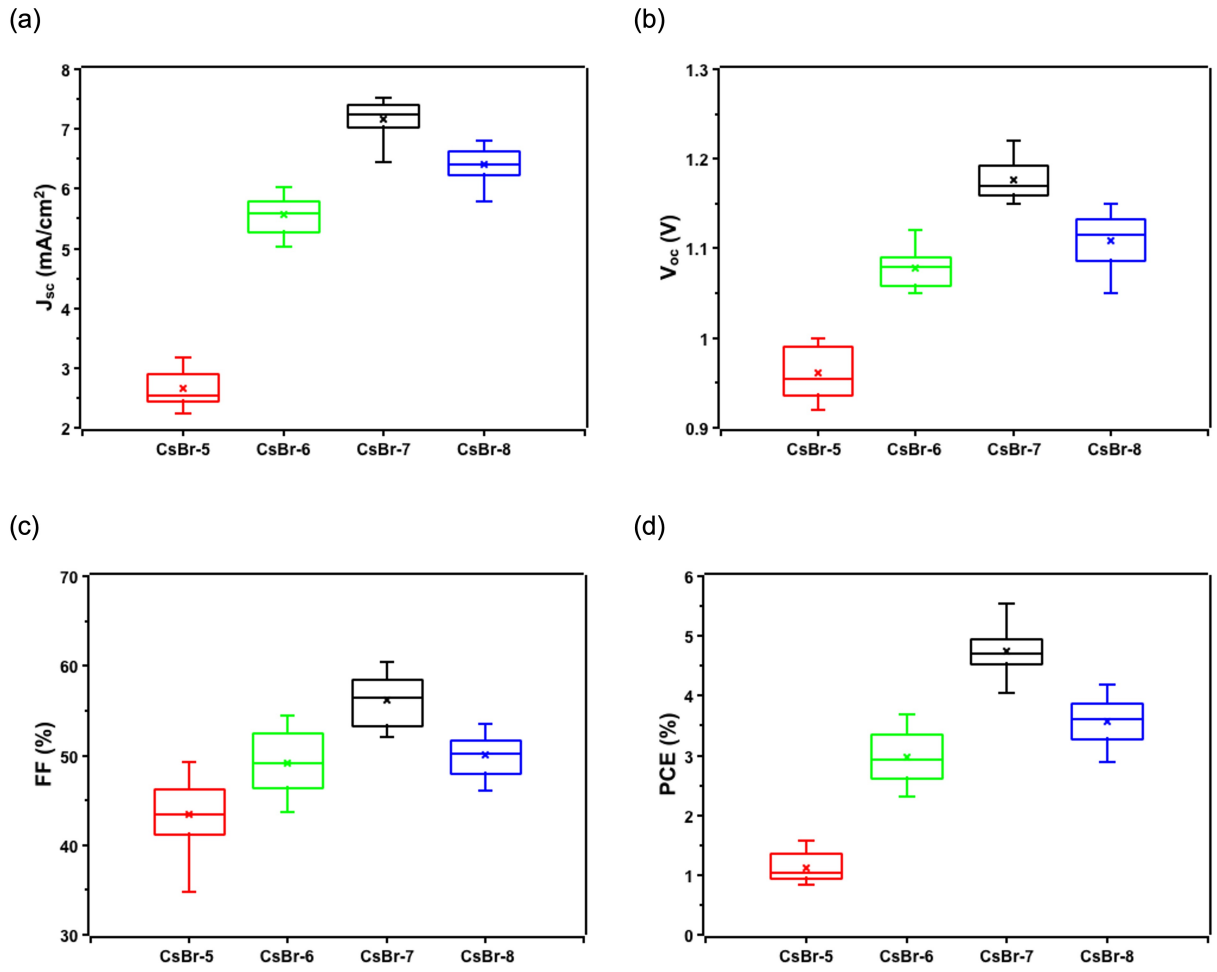

Figure 2.8 Box plots of (a) J_{sc}, (b) V_{oc}, (c) *FF*, and (d) *PCE* of solar cells prepared from different CsBr deposition cycles. Each group has 20 devices.

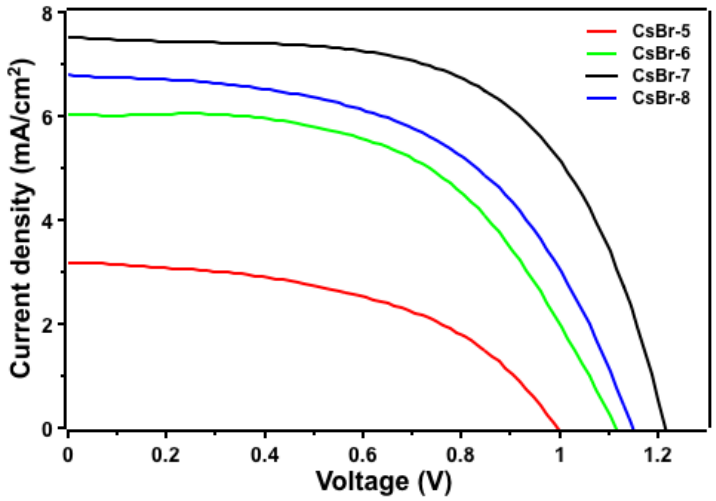

Figure 2.9 J–V curves of the champions in each group

Table 2.4 Photovoltaic parameters of the champions in each group

CsBr deposition cycles	5	6	7	8
J_{sc} (mA cm^{-2})	3.18	6.03	7.52	6.80
V_{oc} (V)	1.00	1.12	1.22	1.15
FF (%)	49.22	54.42	60.49	53.51
PCE (%)	1.57	3.68	5.55	4.18
R_s (Ω)	60.85	55.41	46.77	50.25
R_{rec} (kΩ)	6.02	9.33	16.14	10.83

The current density (J) – voltage (V) curves of solar cells prepared from various CsBr deposition cycles were measured under AM 1.5 G solar spectrum simulator, of which the light intensity is 100 mW cm^{-2}. Each group contained 20 cells. As shown in Figure 2.8, the results of all groups exhibit good reproducibility. The J–V curves of the champions in each group are plotted in Figure

2.9, and the corresponding photovoltaic parameters are summarized in Table 2.4. J_{sc}, V_{oc}, *FF*, and *PCE* increase by increasing the CsBr deposition cycles from 5 to 7. The maximized J_{sc} (7.52 mA cm^{-2}), V_{oc} (1.22 V), *FF* (60.49%), and *PCE* (5.55%) are obtained after 7 cycles of CsBr deposition. However, further increasing the deposition cycles to 8 causes a decreased photovoltaic performance, with a J_{sc} of 6.80 mA cm^{-2}, V_{oc} of 1.15 V, *FF* of 53.51%, and *PCE* of 4.18%. This trend coincides with XRD and UV-vis absorption results.

The interface charge behavior in solar cells prepared from different CsBr deposition cycles was tracked by the non-disruptive technique EIS. Measurements were conducted in the frequency range from 5 MHz to 1 Hz at a bias of 1.0 V under dark conditions. Figure 2.10 shows Nyquist plots of different devices and the equivalent circuit being used to fit the curves. Normally, the Nyquist plots of a perovskite solar cell consist of two semicircles in the high-frequency part and low-frequency part, respectively. The left semicircle at the higher frequencies reflects the charge transport behavior between perovskite layer and blocking layer interfaces (R_{ct} in Figure 2.10 (b)), which may be undistinguished without illumination because of the limited carrier transfer processes [82–83]. The right semicircle at the lower frequencies illustrates the interfacial recombination and bulk recombination of the device, standing by R_{rec} in Figure 2.10 (b) [84].

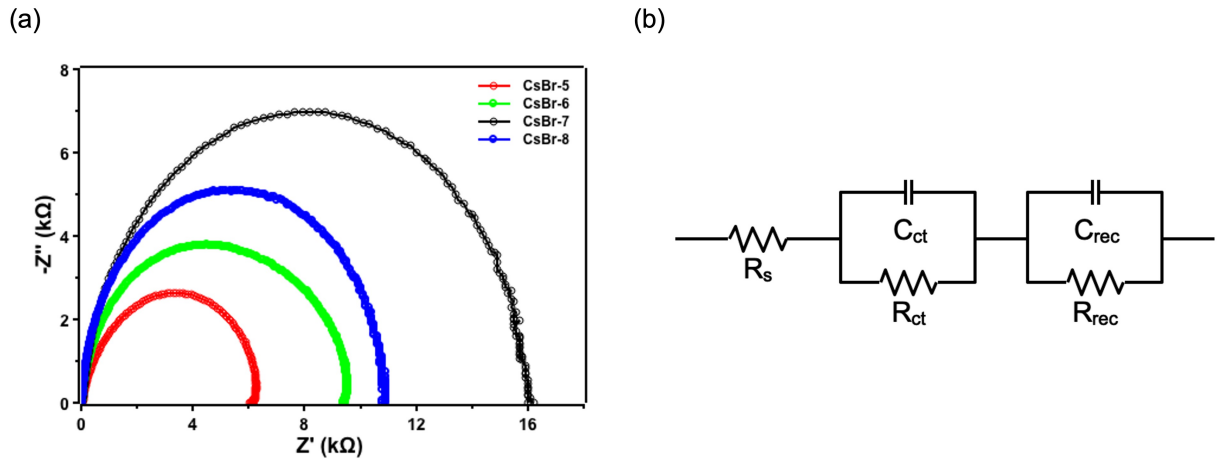

Figure 2.10 (a) Nyquist plots of EIS measurements for solar cells prepared from different CsBr deposition cycles, and (b) the equivalent circuit model for EIS analysis

As shown in Figure 2.10 (a), only one distinct semicircle can be found in the Nyquist plots of the device. The impedance of the circuit is defined as the following equation:

$$Z = R_s + \frac{R_{rec} \times \frac{1}{\omega C_{rec} j}}{R_{rec} + \frac{1}{\omega C_{rec} j}} = R_s + \frac{R_{rec}}{1 + R_{rec}^2 \omega^2 C_{rec}^2} - \frac{R_{rec}^2 \omega C_{rec}}{1 + R_{rec}^2 \omega^2 C_{rec}^2} j$$

where Z, R_s, R_{rec}, C_{rec}, and ω are the impedance, series resistance, recombination resistance, recombination capacitance, and angular frequency, respectively. The resistance of the circuit is represented by the real part of the Nyquist plot:

$$Z' = R_s + \frac{R_{rec}}{1 + R_{rec}^2 \omega^2 C_{rec}^2}$$

When ω approaches positive infinity, Z' approaches R_s. When ω approaches zero, Z' approaches $R_s + R_{rec}$. Therefore, the left intercept point at the real part of the Nyquist plots represents the series resistance of the device (R_s in Figure 2.10 (b)), and the diameter of the semicircle corresponds to the recombination resistance R_{rec} [82].

The series resistance and recombination resistance of different devices are summarized in Table 2.4. As CsBr deposition cycles increase from 5 to 7, the series resistance slightly decreases and the recombination resistance significantly increases. The smallest series resistance and the largest recombination resistance are achieved at the CsBr-7 device, corresponding to the highest photocurrent [85] and the lowest charge recombination rate, respectively. However, as the CsBr deposition cycles further increase to 8, increased series resistance and decreased recombination resistance are observed, possibly resulting from the higher defect density and longer charge migration distance [85–86]. This aligns with the J–V curve results and XRD results, that the charges can move more smoothly in samples with higher crystallization and less unfavorable mixed phases.

To evaluate the possibility of using inorganic CuSCN as an alternative to organic Spiro-OMeTAD hole transporting material in $CsPbBr_3$-based perovskite solar cell, the structure and photovoltaic parameters of some reported devices are summarized in Table 2.5 for comparison. The champion in this research exhibits comparable J_{sc} and slightly lower V_{oc} to that of Spiro-OMeTAD based devices, revealing that CuSCN has the potential to replace Spiro-OMeTAD for hole transport. However, the unsatisfactory *FF* is the culprit for the relatively low *PCE*. The *FF* is determined by the parasitic resistances of the device, which can be calculated from the J–V curve. The inverse slope of the curve at the x-intercept and y-intercept represents the series resistance (R_s) and shunt resistance (R_{sh}), respectively. As shown in Table 2.5, higher series resistance and lower shunt resistance are obtained in this work, probably introduced by imperfect film thickness and quality, or higher recombination rate through a higher density of defect sites at the heterojunction between layers [87], which should be solved in the future study.

Table 2.5 Summary of photovoltaic parameters of $CsPbBr_3$-based perovskite solar cells in the literature

Device	J_{sc} (mA cm^{-2})	V_{oc} (V)	FF (%)	PCE (%)	R_s (Ω cm^2)	R_{sh} (kΩ cm^2)	Ref.
FTO/TiO_2/$CsPbBr_3$/Spiro-OMeTAD/Au	6.75	1.00	74	4.98	284.92	103.60	[64]
FTO/TiO_2/$CsPbBr_3$/Spiro-OMeTAD/Ag	7.14	0.98	71.9	5.04	193.90	45.38	[88]
FTO/TiO_2/$CsPbBr_3$/Spiro-OMeTAD/Au	6.52	1.34	69	6.05	181.27	48.62	[89]
FTO/TiO_2/$CsPbBr_3$/Spiro-OMeTAD/Au	6.97	1.27	78.5	6.95	96.67	74.52	[90]
FTO/ZnO/$CsPbBr_3$/Spiro-OMeTAD/Au	7.01	1.44	77.11	7.78	58.73	55.40	[39]
ITO/ZnO/$CsPbBr_3$/CuSCN/Au	7.52	1.22	60.49	5.55	294.52	34.73	This work

2.4 Conclusion

In this chapter, the two-step solution processing technique provides a strategy for preparing thick and uniform $CsPbBr_3$ film. To obtain $CsPbBr_3$ film with high phase purity, large grains, and strong absorption, optimization was made on the number of CsBr deposition cycles. Based on the as-prepared $CsPbBr_3$ film, an all-inorganic perovskite solar cell with a *PCE* of 5.55% was fabricated in an ambient environment, by using low-temperature solution-processed CuSCN hole transporting material. In comparison to Spiro-OMeTAD-based $CsPbBr_3$ perovskite solar cells in the literature, the device exhibits comparable J_{sc} of 7.52 mA cm^{-2} and slightly lower V_{oc} of 1.22 V,

while the unsatisfactory *FF* of 60.49% is the culprit for the relatively low *PCE*. In contrast to expensive Spiro-OMeTAD which needs the addition of p-dopants to reach its peak performance, CuSCN can act as an effective hole transporting material without any additives. The results show that CuSCN has the potential to replace Spiro-OMeTAD as hole transporting material in terms of photovoltaic performance, but more efforts need to be made to improve the low *FF* of the device.

Chapter 3: Stability performance of all-inorganic perovskite solar cell

3.1 Introduction

Although stable $CsPbBr_3$ material improves the stability of perovskite solar cells, the widely used Spiro-OMeTAD hole transporting material still causes degradation, due to the poor tolerance of LiTFSI and 4-tBP additives against harsh environments. The inexpensive CuSCN p-type semiconductor can be an ideal alternative, owing to its chemical stability and unique electronic properties. In the previous chapter, the photovoltaic performance of CuSCN-based $CsPbBr_3$ perovskite solar cell was evaluated. In this chapter, device stability is investigated in terms of four factors: air (oxygen and moisture) stability, UV stability, temperature dependence, and thermal stability. Comparisons to results in the literature are presented as well.

3.2 Experimental section

Air stability test: The as-fabricated 7 devices without encapsulation were stored in an ambient environment with 30–50% humidity at 20 °C for 60 days.

UV stability test: The as-fabricated 7 devices without encapsulation were stored under 10 mW cm^{-2} of UV light with a wavelength of 365 nm for 8 h day^{-1} for 30 days.

Temperature dependence test: The as-fabricated 10 devices without encapsulation were stored at different temperatures for 30 min.

Thermal stability test: The as-fabricated 5 devices without encapsulation were stored at 70 °C under 10–20% RH for 30 days.

3.3 Results and discussion

3.3.1 Air stability

Caused by hydration and oxidation in ambient air, the degradation of perovskite materials is the main factor affecting the air stability of perovskite solar cells, especially for hybrid organic-inorganic perovskites. Besides, the organic Spiro-OMeTAD hole transporting layer also suffers from degradation under long-term exposure to air. Here, the air stability of the as-fabricated all-inorganic device is investigated and compared to that of other devices in the literature.

As shown in Figure 3.1, only an average of 9% loss is witnessed in the as-fabricated all-inorganic devices within 60 days. It is well noticed that J_{sc} increases slightly after 30 days, possibly caused by the oxygen in the air. There exists competition between electron-donor and electron-acceptor in $CsPbBr_3$ film driven by oxygen adsorption. Br vacancies in $CsPbBr_3$ film act as electron donors, occupied by oxygen molecules that provide holes. As $CsPbBr_3$ is a p-type semiconductor, the adsorption of oxygen leads to the increases of hole carriers and conductance [91]. In addition, the adsorbed oxygen can serve as a passivator suppressing the defect density and nonradiative recombination in $CsPbBr_3$ film by reducing trap states [92]. These can be possible explanations for the increase of J_{sc}.

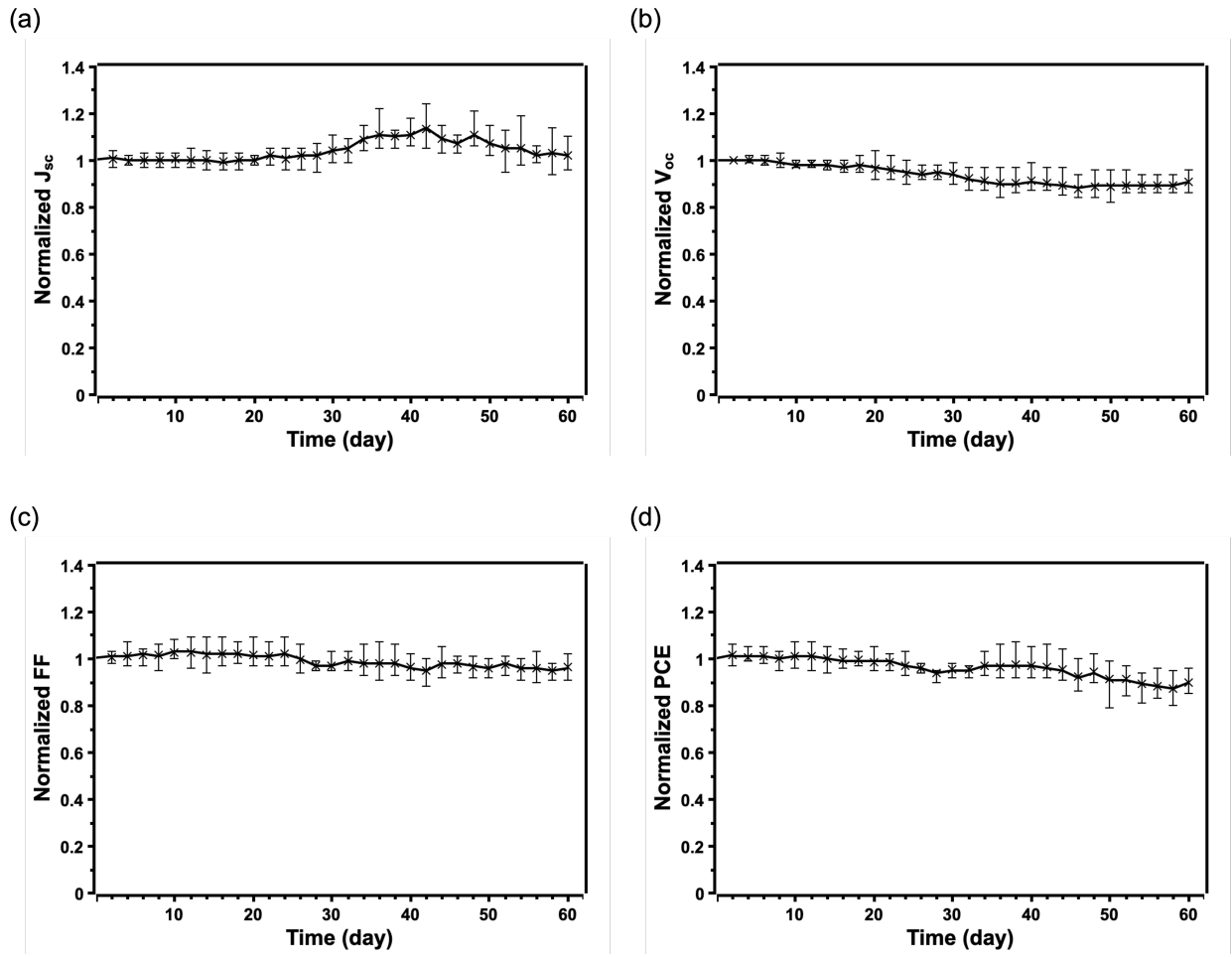

Figure 3.1 Normalized (a) J_{sc}, (b) V_{oc}, (c) *FF*, and (d) *PCE* of perovskite solar cells without encapsulation stored in an ambient environment with 30–50% humidity at 20 °C for 60 days. The traces correspond to the average values of 7 devices.

Table 3.1 illustrates the air stability test results of other devices in the literature. In comparison, the all-inorganic perovskite solar cell in this work exhibits improved air stability, which benefits from the use of inorganic components including $CsPbBr_3$ photoactive material and CuSCN hole transporting material.

Table 3.1 A comparison to the air stability test results of perovskite solar cells in the literature

Device structure	Test condition	Efficiency loss	PCE	Ref.
ITO/ZnO/$MAPbI_3$/Spiro-OMeTAD/Ag	480 h, air	8%	13.9%	[93]
FTO/TiO_2/$MAPbI_3$-2% $CsPbBr_3$/Spiro-OMeTAD/Au	500 h, 30–40% RH, 25–35 °C	15%	20.46%	[94]
FTO/TiO_2/$CsPbBr_3$/Spiro-OMeTAD/Ag	800 h, air	20%	5.36%	[76]
FTO/TiO_2/$CsPbBr_3$/Spiro-OMeTAD/Ag	1000 h, ~45% RH	~35%	10.91%	[95]
ITO/ZnO/$CsPbBr_3$/CuSCN/Au	1440 h, 30–50% RH, 20 °C, air	9%	5.55%	This work

The chemical decomposition of $MAPbI_3$ is represented by the following chemical equations as an example [96]:

$$CH_3NH_3PbI_3\ (s) \leftrightarrow PbI_2\ (s) + CH_3NH_3I\ (aq)$$

$$CH_3NH_3I\ (aq) \leftrightarrow CH_3NH_2\ (aq) + HI\ (aq)$$

$$4\ HI\ (aq) + O_2\ (g) \leftrightarrow 2I_2\ (s) + 2H_2O$$

$$2HI\ (aq) \leftrightarrow H_2\ (g) + I_2\ (s)$$

The exist of highly polar molecule H_2O causes the breaking of hydrogen bonds between organic and inorganic units in perovskite. $CH_3NH_3PbI_3$ degrades into PbI_2 and CH_3NH_3I, where CH_3NH_3I further decomposes into CH_3NH_2 and HI. The O_2 in ambient air consumes HI and facilitates the whole decomposition reaction [97].

Furthermore, the surface of solution-processed ZnO nanomaterials is usually covered with hydroxyl groups and chemical residuals, which can accelerate the decomposition of the upper perovskites layer [98]:

$$CH_3NH_3PbI_3\ (s) \leftrightarrow PbI_2\ (s) + CH_3NH_3I\ (aq)$$

$$CH_3NH_3I\ (aq) + OH^- \leftrightarrow CH_3NH_3OH\ (aq) + I^-\ (aq)$$

$$CH_3NH_3OH\ (aq) \leftrightarrow CH_3NH_2\ (aq) + H_2O\ (aq)$$

In contrast, inorganic Cs^+ cation has lower hydrophilicity and volatility, and thus is less sensitive to the components in ambient air. Besides, the replacement of I^- by Br^- which has smaller ionic radii further enhances the phase stability. As a result, $CsPbBr_3$ shows outstanding stability in ambient air.

The inorganic CuSCN hole transporting layer also has a positive effect on the air stability of the device. The most popular hole transporting material Spiro-OMeTAD is typically doped by p-dopant LiTFSI to improve the hole mobility and electrical conductivity. The hygroscopicity of LiTFSI makes perovskite solar cells vulnerable to moisture [44]. Apart from the hygroscopicity, aging and deterioration of organic components can also lead to device instability. In contrast, the air stability of the device is enhanced by using CuSCN hole transporting material.

3.3.2 UV stability

The AM 1.5G solar spectral irradiation contains about 4.6 mW cm^{-2} of UV light at wavelengths below 400 nm [34], which is the cause of performance degradation of perovskite solar cells during

long-term light soaking. To investigate the UV stability performance of the as-fabricated all-inorganic perovskite solar cell, 7 devices were exposed under 10 mW cm^{-2} of UV light with a wavelength of 365 nm for 8 h day^{-1} for 30 days, resembling the UV irradiation of 2 suns for 30 diurnal cycles. As shown in Figure 3.2, the devices remain highly stable during this period. J_{sc} fluctuates around the initial value, and the contributors to the 7% decrease of *PCE* in average are the slight drop of V_{oc} and *FF*.

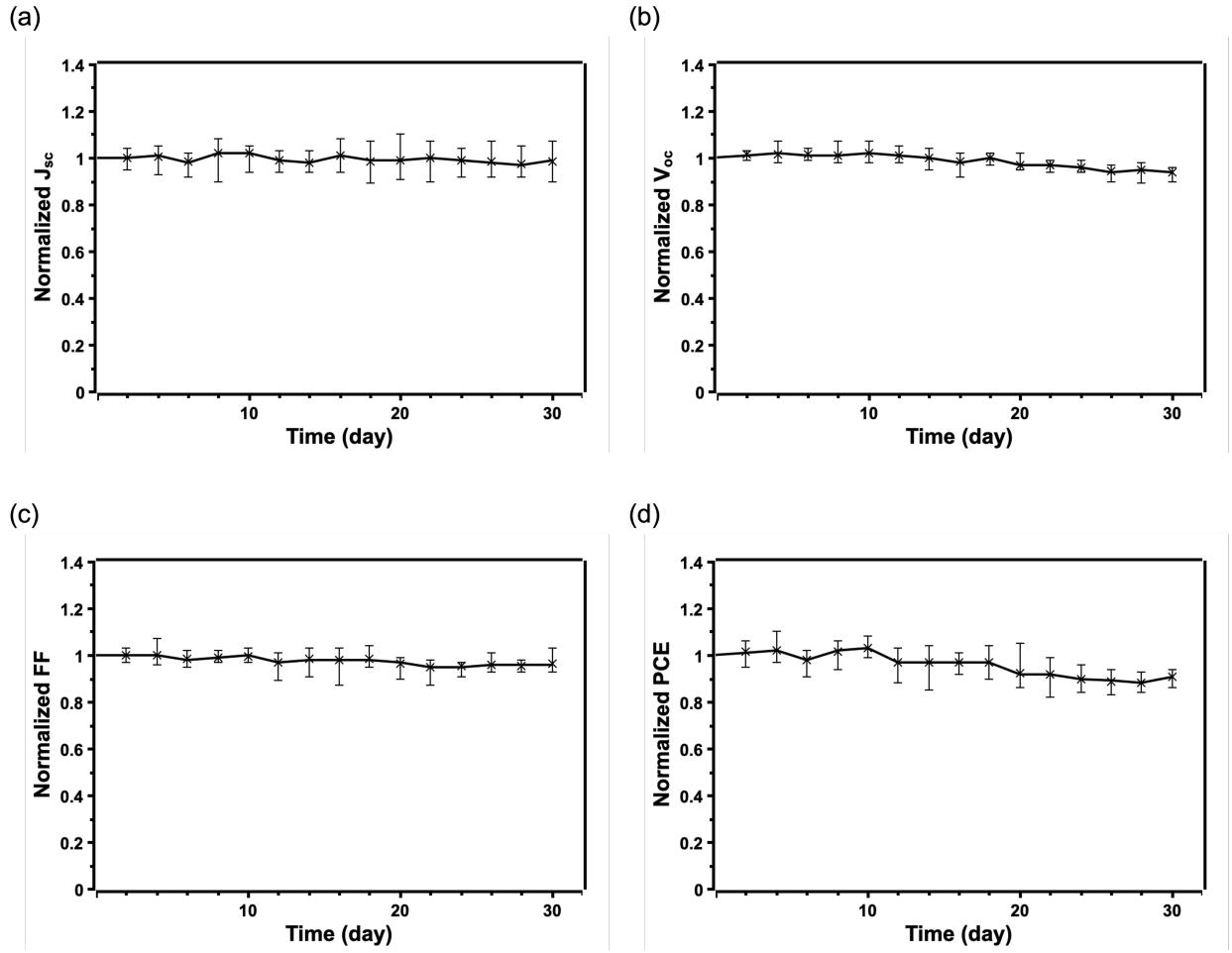

Figure 3.2 Normalized (a) J_{sc}, (b) V_{oc}, (c) *FF*, and (d) *PCE* of perovskite solar cells without encapsulation stored under 10 mW cm^{-2} of UV light with a wavelength of 365 nm for 8 h day^{-1} for 30 days. The traces correspond to the average values of 7 devices.

Table 3.2 A comparison to the UV stability test results of perovskite solar cells in the literature

Device structure	Test condition	Efficiency loss	PCE	Ref.
FTO/TiO_2/FAI:PbI_2:MABr:$PbBr_2$ = 1.0:1.1:0.20:0.22/Spiro-OMeTAD/Au	5 mW cm^{-2}, 8 h day^{-1}, Ar, 2160 h	30% after 168 h, failed after 720 h	17.31%	[99]
FTO/TiO_2/$MAPbI_3$/Spiro-OMeTAD/Au	7.6 mW cm^{-2}, Ar, 1000 h	60–65% after 750–1000 h	14.12%	[34]
FTO/TiO_2-SnO_2/(CsFAMA)$Pb(I_{1-x}Br_x)_3$ (x = 0.1)/CuSCN/C	1 mW cm^{-2}, N_2, 1000 h	10–15% after 720–1000 h	18.1%	[100]
ITO/ZnO/$CsPbBr_3$/CuSCN/Au	10 mW cm^{-2}, 8 h day^{-1}, Air, 720 h	7% after 720 h	5.55%	This work

Compared to hybrid organic-inorganic perovskite solar cells in the literature, the all-inorganic device in this work demonstrates outstanding tolerance to UV irradiation, as shown in Table 3.2. The photocatalytic effect of the "sun-facing" carrier transporting layer is reported to be the main reason for device degradation during long-term UV irradiation [101][34]. The electron transporting materials such as ZnO and TiO_2 show high photocatalytic activity under UV light with a wavelength less than 400 nm. As in the case of TiO_2, Ti^{3+} oxygen vacancies at the surface of TiO_2 are deep electron-donating sites, which adsorb molecular oxygen in the air. In the presence of UV irradiation, electron-hole pairs are generated, and the hole in the valence band recombines with the electron at the oxygen vacancies, accompanied by the desorbing of molecular oxygen. A free electron and a positively charged oxygen vacancy are left in the conduction band and at the surface of TiO_2 film, respectively. The free electron is trapped at the oxygen vacancy site and

recombined with a hole from p-doped Spiro-OMeTAD hole transporting material, leading to the reduction of photovoltaic performance [101].

UV-induced degradation also occurs in the Spiro-OMeTAD hole transporting layer. Spiro is photo-oxidized to a more stable form $Spiro^+$ both in the ambient environment and inert atmosphere, and this process is accelerated in the presence of additives LiTFSI and tBP. The photovoltaic performance of the device is enhanced during the initial partial oxidization of Spiro-OMeTAD resulting from the increased film conductivity and lowered Fermi level, but dramatically drops after reaching a threshold oxidation degree [102]. In addition, the Spiro-OMeTAD HTL and Au electrode are connected by Au-O bonds, which are broken under long-term UV exposure. The damaged HTL/metal interface leads to increased series resistance and unsmooth hole transporting, and therefore has a negative effect on the device performance [103].

Unlike p-doped Spiro-OMeTAD which provides excessive holes and presents the UV-induced degradation issue, the use of dopant-free CuSCN hole transporting material is likely to reduce the possibility of carrier recombination caused by photocatalytic electron transporting material and reduce the risk of UV-induced degradation of the hole transporting material itself. Besides, the decomposition of $MAPbI_3$ can be accelerated under UV irradiation, through the consumption of HI. By contrast, the intrinsic stability of $CsPbBr_3$ is considered to slow down the photovoltaic performance degradation resulting from the decomposition of the perovskite layer.

3.3.3 Temperature dependence

Temperature plays an important role in the carrier mobility and conductivity of semiconducting materials. The sensitivity of a perovskite solar cell to temperature changes determines its operating temperature range. The temperature dependence of the as-fabricated devices was assessed, which were stored at different temperatures for 30 min. Figure 3.3 shows the normalized photovoltaic parameters versus temperature, where the values at 20 °C are the benchmarks.

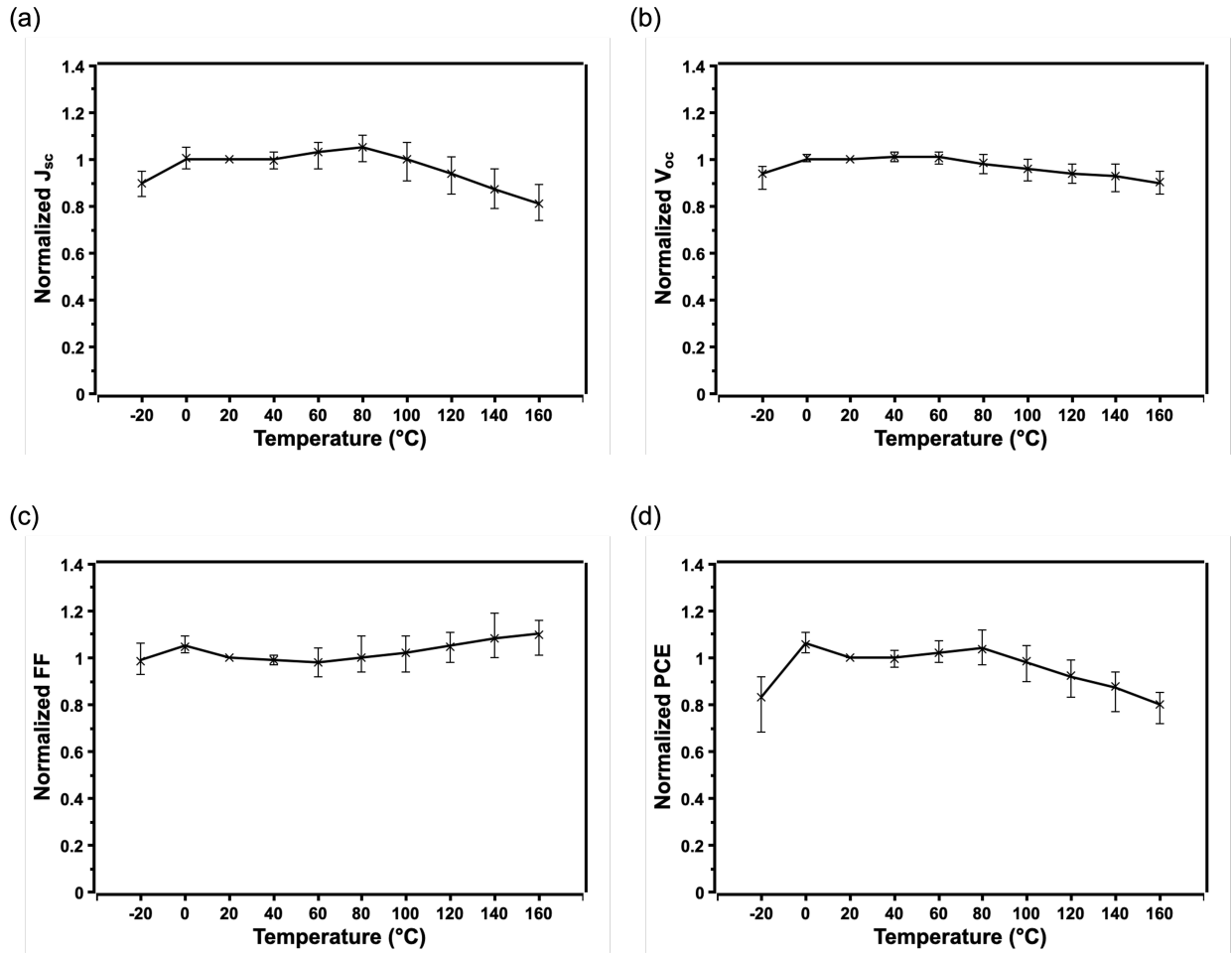

Figure 3.3 Normalized (a) J_{sc}, (b) V_{oc}, (c) *FF*, and (d) *PCE* of perovskite solar cells without encapsulation stored at different temperatures for 30 min. The traces correspond to the average values of 10 devices.

It is shown in Figure 3.3 (a) that, J_{sc} reaches the maximum value at 80 °C, and then decreases. The crystal lattice expansion occurs with increased temperature, and the weakened interatomic bonds cause the bandgap energy reduction. More intrinsic carriers are generated, leading to a slight increase in J_{sc}. However, the crystal lattice expansion also introduces defects in the crystal lattice, which promotes carrier recombination that lowers J_{sc}.

As shown in Figure 3.3 (b), V_{oc} decreases slightly as the temperature increases from 0 °C to 160 °C. A tiny drop of V_{oc} is observed at -20 °C as well, as a consequence of the low carrier mobility. The open-circuit voltage is defined by the following formula:

$$V_{OC} = \frac{nkT}{q} ln\,(\frac{I_L}{I_0} + 1),$$

where n, k, T, q, I_L, and I_0 stand for the diode ideality factor, Boltzmann constant, temperature, elementary charge, photocurrent, and dark saturation current, respectively. Compared with I_L which has relatively small variations at different temperatures, I_0 varies by orders of magnitude, and therefore dominates the change of V_{oc}. I_0 measures the carrier recombination rate of a device. As the temperature increase, more minority carriers diffuse and eventually recombine with majority carriers, contributing to an increase in I_0.

Influenced by parasitic resistance, *FF* shows more complex behavior (Figure 3.3 (c)). The series resistance reduces with temperature rise, resulting from the improved conductivity of charge transporting layers. Meanwhile, the thermally activated charge recombination lowers the shunt resistance, which has a negative effect on *FF* [104]. In general, *FF* almost does not degrade between -20 °C and 160 °C, and is even slightly higher at 0 °C and 160 °C.

The change of J_{sc}, V_{oc}, and *FF* leads to the fluctuation of *PCE* (Figure 3.3 (d)). The highest values are achieved at 0 °C and 80 °C, and decrease is witnessed at both low temperature (< 0 °C) and high temperature (> 80 °C). Despite a few fluctuations, the average *PCE* maintains by 80% at the temperature range of -20–160 °C, indicating the temperature robustness of the device.

Table 3.3 A comparison to the operating temperature of perovskite solar cells in the literature

Device structure	**Operating temperature**	**PCE**	**Ref.**
FTO/TiO_2/$MAPbI_3$/Au	22–75 °C	7.7%	[105]
FTO/TiO_2/$MAPbBr_3$/Spiro-OMeTAD/Au	20–107 °C	7.07%	[106]
FTO/TiO_2/$MAPbI_3$-2% $CsPbBr_3$/Spiro-OMeTAD/Au	0–160 °C	20.46%	[94]
ITO/ZnO/$CsPbBr_3$/CuSCN/Au	-20–160 °C	5.55%	This work

The operating temperature ranges of some reported perovskite solar cells are summarized in Table 3.3. It is noted that here for intuitive comparison, the temperature range at which a device maintains more than 80% of the initial *PCE* is considered as the effective operating temperature range. In comparison, a broader operating temperature range is achieved in this work. Normally, photovoltaic parameters of a material with higher bandgap energy exhibit smaller temperature dependence [107]. According to the UV-vis spectrum result, the $CsPbBr_3$ film has a wider bandgap of 2.36 eV compared with 1.63 eV of $MAPbI_3$ and 2.21 eV of $MAPbBr_3$ [108], which is responsible for the broader operating temperature range. Phase transition of the perovskite layer is another contributing factor for the change of photovoltaic parameters. $CsPbBr_3$ possesses

orthorhombic γ-phase at room temperature, which converts to tetragonal β-phase and cubic α-phase at 88 °C and 130 °C, respectively. However, the three phases show similar properties, indicating the stability of $CsPbBr_3$ in a wide temperature range [25].

In addition to the perovskite layer, the intrinsic stability of the inorganic crystalline structure of blocking layers also contributes to the less significant change of the device performance at higher temperatures. Inorganic CuSCN hole transporting material appears to be thermally stable in comparison with organic blocking material Spiro-OMeTAD, of which the glass transition occurs at low temperature (125 °C). Essential chemical doping of Spiro-OMeTAD with LiTFSI and 4-tBP induces the crystallization of Spiro-OMeTAD and even further reduces the glass transition temperature to 116 °C [109]. As a relatively hard matter, CuSCN is believed to be more effective to protect the perovskite layer against thermal stress [110].

3.3.4 Thermal stability

During normal operation, direct exposure of a solar cell to full sunlight will cause the accumulation of heat into the solar panel. The stability of such devices continuously working at high temperatures is a concern, which can reach up to 85 °C. Here, the long-term thermal stability of the as-fabricated devices was investigated, at a temperature of 70 °C in dark.

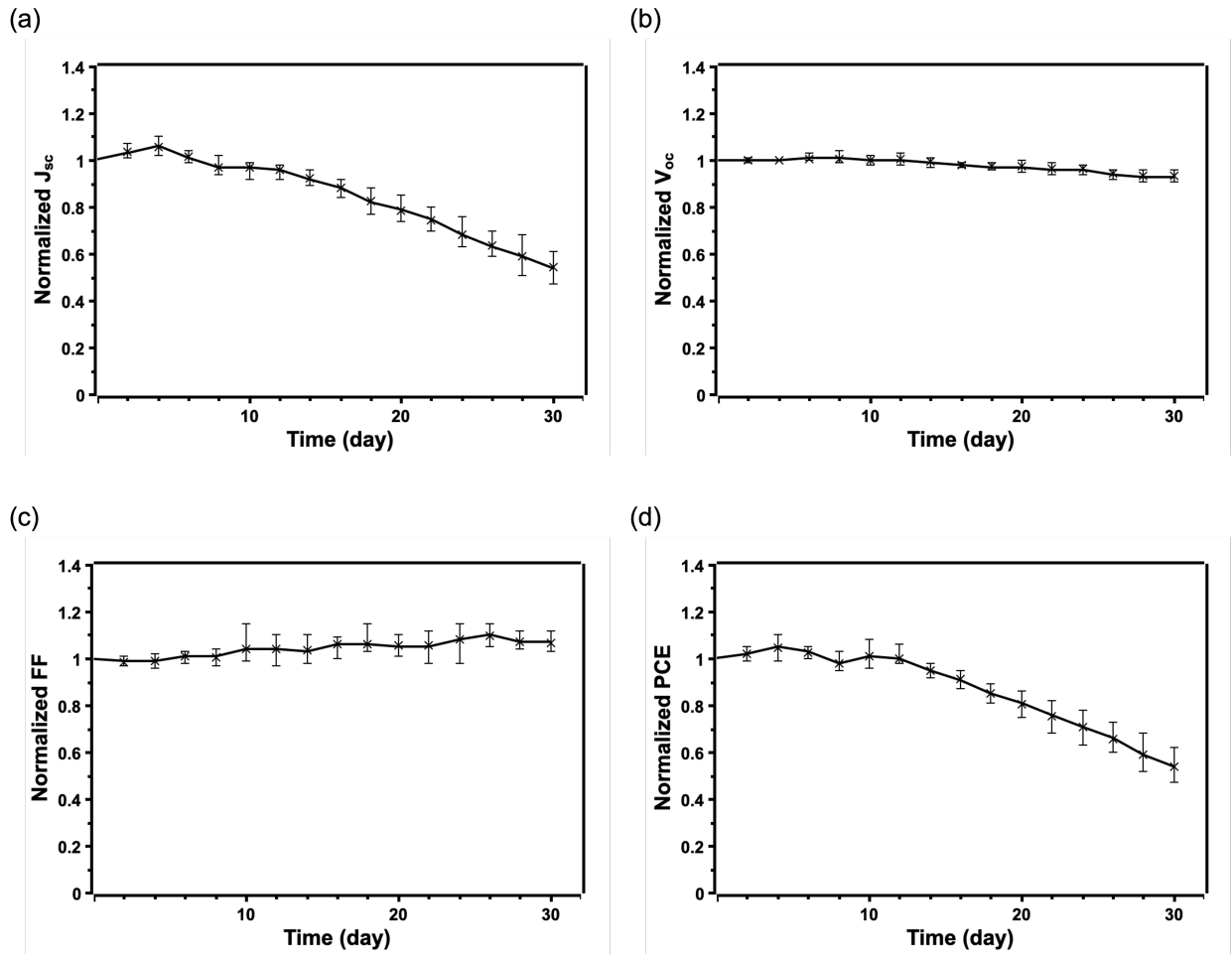

Figure 3.4 Normalized (a) J_{sc}, (b) V_{oc}, (c) *FF*, and (d) *PCE* of perovskite solar cell without encapsulation stored at 70 °C under 10–20% RH for 30 days. The traces correspond to the average values of 5 devices.

As shown in Figure 3.4, the devices do not exhibit the same stability as they performed at room temperature. Although V_{oc} and *FF* still maintain values closing to the initial level, a substantial reduction of J_{sc} is observed, resulting in a loss of 46% in average in *PCE*. Domanski *et al.* reported the diffusion of Au from the electrode across the hole transporting layer into the perovskite layer at temperatures over 70 °C [112]. Since the work function of Au (-5.1 eV) is located between the

VBM (-5.6 eV) and CBM (-3.3 eV) of $CsPbBr_3$, the Au clusters diffused into the perovskite layer act as the electron trap sites [51][113], leading to the formation of shunting pathways that activate the degradation of the device (Figure 3.5). In spite of the inevitable performance loss caused by thermal stress in the perovskite layer during continuous heating, considering that carbon-based $CsPbBr_3$ devices show outstanding thermal stability in previous research [67][111] (Table 3.4), the diffusion of Au electrode is probably the chief factor to the unsatisfactory performance reduction of devices in this work.

Table 3.4 A comparison to the thermal stability test results of perovskite solar cells in the literature

Device structure	Test condition	Efficiency loss	PCE	Ref.
FTO/TiO_2/$CsPbBr_3$/C	80 °C, zero humidity, 960 h	Almost no degradation	7.54%	[67]
FTO/TiO_2/$CsPbBr_3$/C	80 °C, 10–20% RH, 1080 h	Almost no degradation	6.1%	[111]
ITO/ZnO/$CsPbBr_3$/CuSCN/Au	70 °C, 10–20% RH, 720 h	46%	5.55%	This work

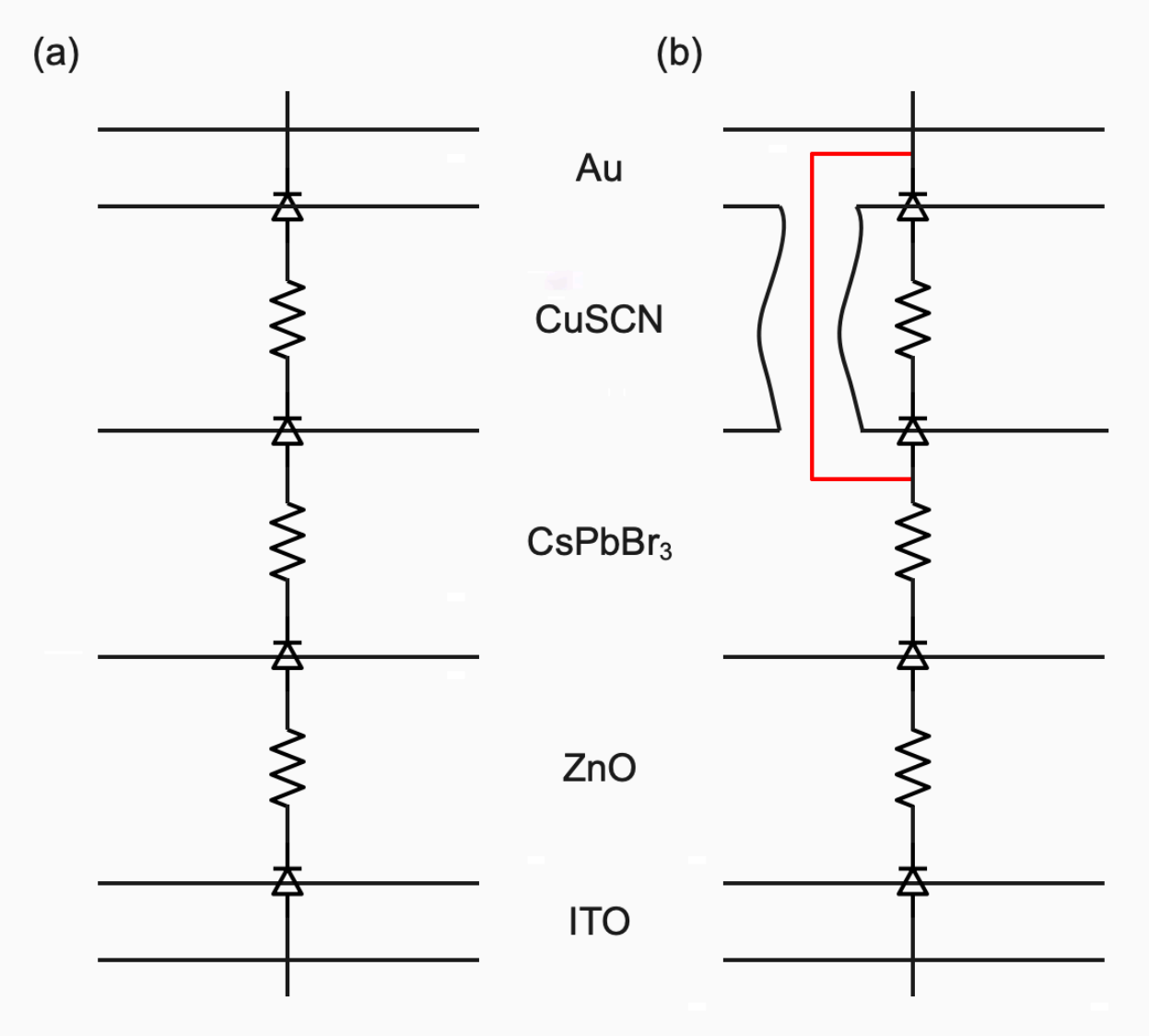

Figure 3.5 Equivalent circuits of the solar cell (a) before and (b) after aging at 70 °C

Even so, in comparison to the $CsPbBr_3$ devices with evaporated Au or Ag metal electrodes, the main disadvantage of HTL-free carbon-based $CsPbBr_3$ devices is the poor adhesion between the carbon film and the substrate [114]. Consisting of carbon power (graphite and carbon black), curing resin, and moderate solvent, conductive carbon paste is the most commonly used carbon electrode, which can be deposited on the perovskite layer through doctor-blading, inkjet printing,

etc. [115–116] However, the large surface roughness of carbon film that results from the agglomeration of carbon is detrimental to the electrical and mechanical contact between perovskite and carbon electrode interface, which is of great importance in the fabrication of large-area devices [115].

EIS of the device before and after aging is presented as Nyquist plots in Figure 3.6. Measurements were conducted in the frequency range from 5 MHz to 1 Hz at a bias of 1.0 V under dark conditions. The values of series resistance (R_s) and recombination resistance (R_{rec}) determined from the Nyquist plots are listed in Table 3.5. A significant reduction can be found in the diameter of the semicircle, corresponding to increased carrier recombination in the device after aging. R_s increases after aging, indicating a less smooth transfer of charge. All these factors contribute to the dramatic drop of J_{sc} in the aged device.

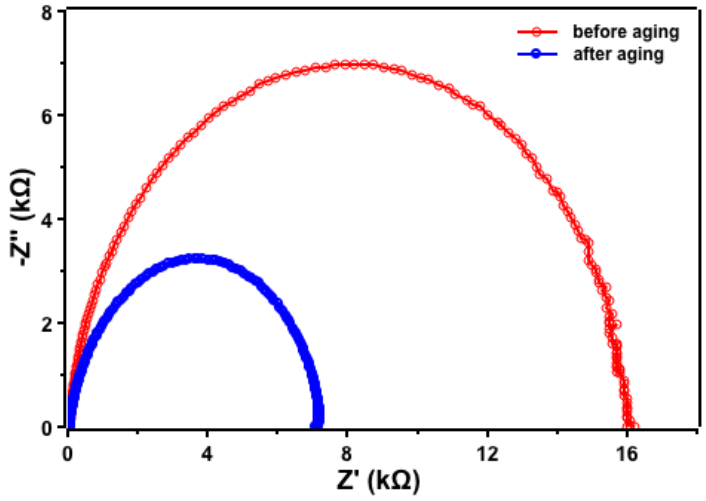

Figure 3.6 Nyquist plots of EIS measurements for the solar cell before and after 30-day aging at 70 °C

Table 3.5 Series resistance (R_s) and charge recombination resistance (R_{rec}) values of the solar cell before and after 30-day aging at 70 °C

Sample	R_s (Ω)	R_{rec} (kΩ)
Before aging	46.77	16.14
After aging	68.49	7.06

3.4 Conclusion

In this chapter, a variety of stability tests on the as-fabricated all-inorganic perovskite solar cell without encapsulation were conducted in different conditions. The working temperature of the device was -20–160 °C. The average loss of *PCE* was 9% in an ambient environment with 30–50% humidity at 20 °C after 60-day aging, 7% under 10 mW cm^{-2} of UV light with a wavelength of 365 nm for 8 h day^{-1} after 30-day aging, and 46% at 70 °C under 10–20% RH after 30-day aging, respectively. In comparison to hybrid organic-inorganic perovskite solar cells or $CsPbBr_3$ perovskite solar cells with Spiro-OMeTAD hole transporting material in the literature, the all-inorganic perovskite solar cell in this work presented improved air stability and UV stability, and was less temperature-dependent over a broader temperature range. The intrinsically stable crystalline structure of $CsPbBr_3$ and dopant-free CuSCN could mainly contribute to it. However, faster degradation was witnessed during thermal aging compared to carbon-based $CsPbBr_3$ devices in the literature, possibly resulting from the diffusion of Au electrode.

Chapter 4: Conclusion and outlook

During the past decade, perovskite solar cell has become a research hotspot in the photovoltaic field. Despite the considerable breakthroughs researchers made, device stability is one of the main challenges to the commercial-scale application of perovskites. Highly stable $CsPbBr_3$ material has the potential to provide solutions for this issue. As the heart of a perovskite solar cell, a high-quality $CsPbBr_3$ layer is of great importance to the device stability and performance, which requires reliable and reproducible film preparation techniques. Apart from the perovskite layer, the device stability also relies on other components of a cell. Widely used Spiro-OMeTAD hole transporting material suffers from degradation, and the prohibitively high cost limits its large-scale application. The inexpensive CuSCN inorganic p-type semiconductor is considered to be a promising alternative. This work focuses on the preparation and optimization of $CsPbBr_3$ film, as well as the evaluation of stability and performance of $CsPbBr_3$ perovskite solar cell with CuSCN hole transporting material:

(1) The solution-processed technique is a simple and low-cost strategy for perovskite film preparation. In the one-step solution method, the low solubility of CsBr precursor in commonly used solvents leads to thin and ununiform $CsPbBr_3$ films. To overcome the solubility difference issue between CsBr and $PbBr_2$, the two-step solution technique was adopted for the fabrication of $CsPbBr_3$ film. By optimizing the number of CsBr deposition cycles, $CsPbBr_3$ film with high phase purity, large grains, and strong absorption was obtained.

(2) Based on the as-prepared $CsPbBr_3$ film, $CsPbBr_3$ perovskite solar cells were fabricated in an ambient environment, using low-temperature solution-processed CuSCN as hole transporting material. The best device achieved a J_{sc} of 7.52 mA cm^{-2}, a V_{oc} of 1.22 V, a *FF* of 60.49%, and a *PCE* of 5.55%, demonstrating the ability of CuSCN on efficient hole extraction in $CsPbBr_3$ perovskite solar cells. Compared to Spiro-OMeTAD-based devices in the literature, it presented comparable J_{sc} and V_{oc}, while the *PCE* was yet slightly lower because of the unsatisfactory *FF*. Moreover, the device exhibited a broader working temperature of -20–160 °C and improved long-term stability in the ambient environment or under UV exposure, in comparison to hybrid organic-inorganic perovskite solar cells or Spiro-OMeTAD-based $CsPbBr_3$ perovskite solar cells in the literature. However, faster degradation was witnessed during thermal aging compared to carbon-based $CsPbBr_3$ devices in the literature, possibly resulting from the diffusion of Au electrode. In addition, according to the information from Sigma Aldrich, the price of CuSCN (CA$2.43 per gram) [117] was dramatically lower than that of Spiro-OMeTAD (CA$432 per gram) [118], making it more promising for commercialization.

This work provides a pathway for the large-scale fabrication of efficient, stable, and inexpensive perovskite solar cells. The following research directions are identified from this work:

(1) Developing advanced preparation techniques for $CsPbBr_3$ film and optimizing charge transporting layers are essential to enhance the photovoltaic performance of the $CsPbBr_3$-based device. In this work the unsatisfactory *FF* of the device was the culprit for the relatively low *PCE*, possibly owing to imperfect film quality or the higher recombination rate through a

higher density of defect sites at the interfaces. Although the two-step solution method solves the solubility difference issue between CsBr and $PbBr_2$, impurities still exist in $CsPbBr_3$ film, and defects are inevitably produced during high-temperature annealing and rapid crystallization process. Moreover, attention should be drawn to the optimization of the electron transporting layer and hole transporting layer in various aspects, including charge mobility, trap states, interfacial properties, and energy level alignment.

(2) Solving the infiltration of the metal electrode and understanding the degradation mechanism are important for improving the device stability. A buffer layer can be introduced between the perovskite layer and the metal electrode to avoid metal infiltration. Replacing the expensive gold electrode with stable and inexpensive carbon electrodes may be another strategy to enhance the thermal stability of the device, and the hydrophobic carbon electrode can also be a moisture barrier against a high humidity environment, but the problem of poor adhesion of carbon electrodes needs to be solved by specific methods such as surface modification and improved preparation techniques. In this work, stability tests were conducted in different operating conditions, but the mechanism of degradation is still unclear, possibly caused by interfacial chemical reactions between each layer.

(3) New designs are needed to balance the *PCE* and stability. In spite of the high stability $CsPbBr_3$ performs, its large bandgap of 2.3 eV limits the *PCE* of $CsPbBr_3$-based perovskite solar cells. Fabricating tandem solar cells combining $CsPbBr_3$ and smaller bandgap photovoltaic materials can be one approach to breaking the *PCE* limit without sacrificing stability.

Bibliography

[1] OPEC, 2021. *2021 World Oil Outlook 2045*. Available at: https://woo.opec.org/chapter.php?chapterNr=12&tableID=66 [Accessed November 22, 2021].

[2] Thirugnanasambandam, M., Iniyan, S. & Goic, R., 2010. A review of Solar Thermal Technologies. *Renewable and Sustainable Energy Reviews*, 14(1), pp.312–322.

[3] IRENA, 2021. *Renewable Energy Statistics 2021*. Available at: https://irena.org/publications/2021/Aug/-/media/DE99E76D009042DE9A01F724A0CFBE9F.ashx [Accessed November 22, 2021].

[4] NREL, *Best research-cell efficiency chart*. Available at: https://www.nrel.gov/pv/cell-efficiency.html [Accessed November 22, 2021].

[5] Nijs, J., 2019. Photovoltaic solar energy: Present and future, in Aurelio Peccei Lectures. *The Royal Flemish Academy of Belgium of Sciences and Arts*, pp.1–103.

[6] Lee, T.D. & Ebong, A.U., 2017. A review of thin film solar cell technologies and challenges. *Renewable and Sustainable Energy Reviews*, 70, pp.1286–1297.

[7] Green, M.A., Ho-Baillie, A. & Snaith, H.J., 2014. The emergence of perovskite solar cells. *Nature Photonics*, 8(7), pp.506–514.

[8] Kojima, A. et al., 2009. Organometal halide perovskites as visible-light sensitizers for photovoltaic cells. *Journal of the American Chemical Society*, 131(17), pp.6050–6051.

[9] Mendes, M.J. et al., 2020. Wave-optical front structures on silicon and perovskite thin-film solar cells. *Solar Cells and Light Management*, pp.315–354.

[10] Fu, Q. et al., 2018. Recent progress on the long-term stability of perovskite solar cells. *Advanced Science*, 5(5), p.1700387.

[11] Targhi, F.F., Jalili, Y.S. & Kanjouri, F., 2018. $MAPbI_3$ and $FAPbI_3$ perovskites as solar cells: Case study on structural, electrical and optical properties. *Results in Physics*, 10, pp.616–627.

[12] Amat, A. et al., 2014. Cation-induced band-gap tuning in organohalide perovskites: Interplay of spin–orbit coupling and octahedra tilting. *Nano Letters*, 14(6), pp.3608–3616.

[13] Eperon, G.E. et al., 2014. Formamidinium lead trihalide: A broadly tunable perovskite for efficient planar heterojunction solar cells. *Energy & Environmental Science*, 7, pp.982–988.

[14] Koh, T.M. et al., 2014. Formamidinium-containing metal-halide: An alternative material for near-IR absorption perovskite solar cells. *The Journal of Physical Chemistry C*, 118(30), pp.16458–16462.

[15] Binek, A. et al., 2015. Stabilization of the trigonal high-temperature phase of formamidinium lead iodide. *The Journal of Physical Chemistry Letters*, 6(7), pp.1249–1253.

[16] Li, Z. et al., 2016. Stabilizing perovskite structures by tuning tolerance factor: Formation of formamidinium and cesium lead iodide solid-state alloys. *Chemistry of Materials*, 28(1), pp.284–292.

[17] Lee, J.W. et al., 2015. Formamidinium and cesium hybridization for photo- and moisture-stable perovskite solar cell. *Advanced Energy Materials*, 5(20), p.1501310.

[18] Saliba, M. et al., 2016. Cesium-containing triple cation perovskite solar cells: Improved stability, reproducibility and high efficiency. *Energy & Environmental Science*, 9(6), pp.1989–1997.

[19] Liu, D. et al., 2020. Insight into the improved phase stability of $CsPbI_3$ from first-principles calculations. *ACS Omega*, 5(1), pp.893–896.

[20] Dastidar, S. et al., 2017. Quantitative phase-change thermodynamics and metastability of perovskite-phase cesium lead iodide. *The Journal of Physical Chemistry Letters*, 8(6), pp.1278–1282.

[21] Frolova, L.A. et al., 2017. Highly efficient all-inorganic planar heterojunction perovskite solar cells produced by thermal coevaporation of CsI and PbI_2. *The Journal of Physical Chemistry Letters*, 8(1), pp.67–72.

[22] Trots, D.M. & Myagkota, S.V., 2008. High-temperature structural evolution of caesium and rubidium triiodoplumbates. *Journal of Physics and Chemistry of Solids*, 69(10), pp.2520–2526.

[23] Wang, P. et al., 2018. Solvent-controlled growth of inorganic perovskite films in dry environment for efficient and stable solar cells. *Nature Communications*, 9.

[24] Sanchez, S. et al., 2018. Efficient and stable inorganic perovskite solar cells manufactured by pulsed flash infrared annealing. *Advanced Energy Materials*, 8(30), p.1802060.

[25] Ullah, S. et al., 2021. All-inorganic $CsPbBr_3$ perovskite: A promising choice for photovoltaics. *Materials Advances*, 2(2), pp.646–683.

[26] Duan, J. et al., 2019. Inorganic perovskite solar cells: An emerging member of the photovoltaic community. *Journal of Materials Chemistry A*, 7(37), pp.21036–21068.

[27] Liang, J. et al., 2016. All-inorganic perovskite solar cells. *Journal of the American Chemical Society*, 138(49), pp.15829–15832.

[28] Akbulatov, A.F. et al., 2017. Probing the intrinsic thermal and photochemical stability of hybrid and inorganic lead halide perovskites. *The Journal of Physical Chemistry Letters*, 8(6), pp.1211–1218.

[29] Ogomi, Y. et al., 2014. $CH_3NH_3Sn_xPb_{(1-x)}I_3$ perovskite solar cells covering up to 1060 nm. *The Journal of Physical Chemistry Letters*, 5(6), pp.1004–1011.

[30] Noel, N.K. et al., 2014. Lead-free organic–inorganic tin halide perovskites for photovoltaic applications. *Energy & Environmental Science*, 7(9), pp.3061–3068.

[31] Hao, F. et al., 2014. Lead-free solid-state organic–inorganic halide perovskite solar cells. *Nature Photonics*, 8(6), pp.489–494.

[32] Li, H. et al., 2018. Interface Engineering using a perovskite derivative phase for efficient and stable $CsPbBr_3$ solar cells. *Journal of Materials Chemistry A*, 6(29), pp.14255–14261.

[33] Wu, W.Q. et al., 2017. Recent progress in hybrid perovskite solar cells based on n-type materials. *Journal of Materials Chemistry A*, 5(21), pp.10092–10109.

[34] Lee, S.W. et al., 2016. UV degradation and recovery of perovskite solar cells. *Scientific Reports*, 6, p.38150.

[35] Pathak, S.K. et al., 2014. Performance and stability enhancement of dye-sensitized and perovskite solar cells by al doping of TiO_2. *Advanced Functional Materials*, 24(38), pp.6046–6055.

[36] Zhao, Y. et al., 2019. Using SnO_2 QDs and $CsMBr_3$ (M = Sn, Bi, Cu) QDs as charge-transporting materials for 10.6%-efficiency all-inorganic $CSPbBr_3$ perovskite solar cells with an ultrahigh open-circuit voltage of 1.610 V. *Solar RRL*, 3(3), p.1800284.

[37] Qiu, L. et al., 2019. Scalable fabrication of stable high efficiency perovskite solar cells and modules utilizing room temperature sputtered SnO_2 electron transport layer. *Advanced Functional Materials*, 29(47), p.1806779.

[38] Zhang, X. et al., 2018. All-ambient processed binary $CsPbBr_3$–$CsPb_2Br_5$ perovskites with synergistic enhancement for high-efficiency Cs–Pb–Br-based solar cells. *ACS Applied Materials & Interfaces*, 10(8), pp.7145–7154.

[39] Chen, W. et al., 2018. A semitransparent inorganic perovskite film for overcoming ultraviolet light instability of organic solar cells and achieving 14.03% efficiency. *Advanced Materials*, 30(21), p.1800855.

[40] Luchkin, S.Y. et al., 2017. Spatially-resolved nanoscale measurements of grain boundary enhanced photocurrent in inorganic $CsPbBr_3$ perovskite films. *Solar Energy Materials and Solar Cells*, 171, pp.205–212.

[41] Pont, S. et al., 2018. Stability of polymer:PCBM thin films under competitive illumination and thermal stress. *Advanced Functional Materials*, 28(40), p.1802520.

[42] Leijtens, T. et al., 2012. Hole transport materials with low glass transition temperatures and high solubility for application in solid-state dye-sensitized solar cells. *ACS Nano*, 6(2), pp.1455–1462.

[43] Nguyen, W.H. et al., 2014. Enhancing the hole-conductivity of Spiro-OMeTAD without oxygen or lithium salts by using $Spiro(TFSI)_2$ in perovskite and dye-sensitized solar cells. *Journal of the American Chemical Society*, 136(31), pp.10996–11001.

[44] Pellaroque, A. et al., 2017. Efficient and stable perovskite solar cells using molybdenum tris(dithiolene)s as p-dopants for Spiro-OMeTAD. *ACS Energy Letters*, 2(9), pp.2044–2050.

[45] Kasparavicius, E. et al., 2018. Long-term stability of the oxidized hole-transporting materials used in perovskite solar cells. *Chemistry - A European Journal*, 24(39), pp.9910–9918.

[46] Wang, S., Yuan, W. & Meng, Y.S., 2015. Spectrum-dependent Spiro-OMeTAD oxidization mechanism in perovskite solar cells. *ACS Applied Materials & Interfaces*, 7(44), pp.24791–24798.

[47] Kulbak, M. et al., 2016. Cesium enhances long-term stability of lead bromide perovskite-based solar cells. *The Journal of Physical Chemistry Letters*, 7(1), pp.167–172.

[48] Kim, J. et al., 2017. An effective method of predicting perovskite solar cell lifetime–case study on planar $CH_3NH_3PbI_3$ and $HC(NH_2)_2PbI_3$ perovskite solar cells and hole transfer materials of Spiro-OMeTAD and PTAA. *Solar Energy Materials and Solar Cells*, 162, pp.41–46.

[49] Wang, G. et al., 2019. Improving photovoltaic performance of carbon-based $CsPbBr_3$ perovskite solar cells by interfacial engineering using P3HT interlayer. *Journal of Power Sources*, 432, pp.48–54.

[50] Liu, Z. et al., 2018. Efficient Carbon-based $CsPbBr_3$ inorganic perovskite solar cells by using Cu-phthalocyanine as hole transport material. *Nano-Micro Letters*, 10(2), p.34.

[51] Li, X. et al., 2019. All-inorganic $CsPbBr_3$ perovskite solar cells with 10.45% efficiency by evaporation-assisted deposition and setting intermediate energy levels. *ACS Applied Materials & Interfaces*, 11(33), pp.29746–29752.

[52] Duan, J. et al., 2019. Hole-boosted $Cu(Cr,M)O_2$ nanocrystals for all-inorganic $CsPbBr_3$ perovskite solar cells. *Angewandte Chemie International Edition*, 58(45), pp.16147–16151.

[53] Mehrabian, M. et al., 2019. A highly stable all-inorganic $CsPbBr_3$ perovskite solar cell. *European Journal of Inorganic Chemistry*, 2019(32), pp.3699–3703.

[54] Zhang, H. et al., 2018. Low-temperature solution-processed $CuCrO_2$ hole-transporting layer for efficient and photostable perovskite solar cells. *Advanced Energy Materials*, 8(13), p.1702762.

[55] Pattanasattayavong, P. et al., 2013. Hole-transporting transistors and circuits based on the transparent inorganic semiconductor copper(I) thiocyanate (CuSCN) processed from solution at room temperature. *Advanced Materials*, 25(10), pp.1504–1509.

[56] Pattanasattayavong, P., Promarak, V. & Anthopoulos, T.D., 2017. Electronic properties of copper(I) thiocyanate (CuSCN). *Advanced Electronic Materials*, 3(3), p.1600378.

[57] Bredas, J.L., 2014. Mind the gap! *Materials Horizions*, 1(1), pp.17–19.

[58] Anwar, F. et al., 2017. Effect of different HTM layers and electrical parameters on ZnO nanorod-based lead-free perovskite solar cell for high-efficiency performance. *International Journal of Photoenergy*, 2017, p.9846310.

[59] Islam, M.B. et al., 2017. NiO_x Hole Transport Layer for perovskite solar cells with improved stability and reproducibility. *ACS Omega*, 2(5), pp.2291–2299.

[60] Kim, G.W., Shinde, D.V. & Park, T., 2015. Thickness of the hole transport layer in perovskite solar cells: Performance versus reproducibility. *RSC Advances*, 5(120), pp.99356–99360.

[61] Zhang, T. et al., 2019. Low-temperature processed inorganic perovskites for flexible detectors with a broadband photoresponse. *Nanoscale*, 11(6), pp.2871–2877.

[62] Rakita, Y. et al., 2016. Low-temperature solution-grown $CsPbBr_3$ single crystals and their characterization. *Crystal Growth & Design*, 16(10), pp.5717–5725.

[63] Huang, D. et al., 2019. One-step solution deposition of $CsPbBr_3$ based on precursor engineering for Efficient All-inorganic perovskite solar cells. *Journal of Materials Chemistry A*, 7(39), pp.22420–22428.

[64] Kulbak, M., Cahen, D. & Hodes, G., 2015. How important is the organic part of lead halide perovskite photovoltaic cells? Efficient $CsPbBr_3$ cells. *The Journal of Physical Chemistry Letters*, 6(13), pp.2452–2456.

[65] Teng, P. et al., 2018. Elegant face-down liquid-space-restricted deposition of $CsPbBr_3$ films for efficient carbon-based all-inorganic planar perovskite solar cells. *ACS Applied Materials & Interfaces*, 10(11), pp.9541–9546.

[66] Liu, X. et al., 2019. Boosting the efficiency of carbon-based planar $CsPbBr_3$ perovskite solar cells by a modified multistep spin-coating technique and interface engineering. *Nano Energy*, 56, pp.184–195.

[67] Duan, J. et al., 2018. High-purity inorganic perovskite films for solar cells with 9.72 % efficiency. *Angewandte Chemie*, 130(14), pp.3849–3853.

[68] Jiang, Z. et al., 2018. Light-soaking free organic photovoltaic devices with sol–gel deposited zno and azo electron transport layers. *RSC Advances*, 8(64), pp.36542–36548.

[69] Chen, J. & Park, N.G., 2018. Inorganic Hole transporting materials for stable and high efficiency perovskite solar cells. *The Journal of Physical Chemistry C*, 122(25), pp.14039–14063.

[70] Arora, N. et al., 2017. Perovskite solar cells with CuSCN hole extraction layers yield stabilized efficiencies greater than 20%. *Science*, 358(6364), pp.768–771.

[71] Dursun, I. et al., 2017. $CsPb_2Br_5$ single crystals: Synthesis and characterization. *ChemSusChem*, 10(19), pp.3746–3749.

[72] Li, G. et al., 2016. Shape and phase evolution from $CsPbBr_3$ perovskite nanocubes to tetragonal $CsPb_2Br_5$ nanosheets with an indirect bandgap. *Chemical Communications*, 52(75), pp.11296–11299.

[73] Cha, J.H. et al., 2017. Photoresponse of $CsPbBr_3$ and Cs_4PbBr_6 perovskite single crystals. *The Journal of Physical Chemistry Letters*, 8(3), pp.565–570.

[74] Duan, J. et al., 2018. Lanthanide ions doped $CsPbBr_3$ halides for HTM-free 10.14%-efficiency inorganic perovskite solar cell with an ultrahigh open-circuit voltage of 1.594 V. *Advanced Energy Materials*, 8(31), p.1802346.

[75] Guan, H. et al., 2020. Room temperature synthesis of stable single silica-coated $CsPbBr_3$ quantum dots combining tunable red emission of Ag–In–Zn–S for high-CRI white light-emitting diodes. *Nano Energy*, 67, p.104279.

[76] Zhou, Z.J. et al., 2019. Cu_2ZnSnS_4 quantum dots as hole transport material for enhanced charge extraction and stability in all-inorganic $CsPbBr_3$ perovskite solar cells. *Solar RRL*, 3(4), p.1800354.

[77] Palazon, F. et al., 2017. From $CsPbBr_3$ nano-inks to sintered $CsPbBr_3$–$CsPb_2Br_5$ films via thermal annealing: Implications on optoelectronic properties. *The Journal of Physical Chemistry C*, 121(21), pp.11956–11961.

[78] Tauc, J., Grigorovici, R. & Vancu, A., 1966. Optical properties and electronic structure of amorphous germanium. *physica status solidi (b)*, 15(2), pp.627–637.

[79] Ziabari, A.A. & Ghodsi, F.E., 2011. Synthesis and characterization of nanocrystalline cdzno thin films prepared by sol-gel dip-coating process. *Thin Solid Films*, 520(4), pp.1228–1232.

[80] Wijeyasinghe, N. et al., 2017. Copper(I) thiocyanate (CuSCN) hole-transport layers processed from aqueous precursor solutions and their application in thin-film transistors and highly efficient organic and organometal halide perovskite solar cells. *Advanced Functional Materials*, 27(35), p.1701818.

[81] Tang, M. et al., 2019. Toward efficient and air-stable carbon-based all-inorganic perovskite solar cells through substituting $CsPbBr_3$ films with transition metal ions. *Chemical Engineering Journal*, 375, p.121930.

[82] Li, J. et al., 2015. Enhanced performance in hybrid perovskite solar cell by modification with spinel lithium titanate. *Journal of Materials Chemistry A*, 3(16), pp.8882–8889.

[83] Yan, X. et al., 2018. Optimization of sputtering NiO_x films for perovskite solar cell applications. *Materials Research Bulletin*, 103, pp.150–157.

[84] Yang, Y. et al., 2015. The size effect of TiO_2 nanoparticles on a printable mesoscopic perovskite solar cell. *Journal of Materials Chemistry A*, 3(17), pp.9103–9107.

[85] Zhang, W. et al., 2017. Investigation of triphenylamine (TPA)-based metal complexes and their application in perovskite solar cells. *ACS Omega*, 2(12), pp.9231–9240.

[86] He, C. et al., 2018. Interface Engineering of BCP buffer layers in planar heterojunction perovskite solar cells with NiO_x hole transporting layers. *Frontiers in Physics*, 6, p.99.

[87] Liu, J. et al., 2016. Identification and mitigation of a critical interfacial instability in perovskite solar cells employing copper thiocyanate hole-transporter. *Advanced Materials Interfaces*, 3(22), p.1600571.

[88] Li, B. et al., 2017. $PbCl_2$-tuned inorganic cubic $CsPbBr_3$(Cl) perovskite solar cells with enhanced electron lifetime, diffusion length and photovoltaic performance. *Journal of Power Sources*, 360, pp.11–20.

[89] Tang, K.C., You, P. & Yan, F., 2018. Highly stable all-inorganic perovskite solar cells processed at low temperature. *Solar RRL*, 2(8), p.1800075.

[90] Lei, J. et al., 2018. Efficient planar $CsPbBr_3$ perovskite solar cells by dual-source vacuum evaporation. *Solar Energy Materials and Solar Cells*, 187, pp.1–8.

[91] Xing, W. et al., 2021. Donor–acceptor competition via halide vacancy filling for oxygen detection of high sensitivity and stability by all-inorganic perovskite films. *Small*, 17(40), p.2102733.

[92] Liu, S.C. et al., 2019. Investigation of oxygen passivation for high-performance all-inorganic perovskite solar cells. *Journal of the American Chemical Society*, 141(45), pp.18075–18082.

[93] Song, J. et al., 2015. Efficient and environmentally stable perovskite solar cells based on ZnO electron collection layer. *Chemistry Letters*, 44(5), pp.610–612.

[94] Gao, Y. et al., 2019. $CsPbBr_3$ perovskite nanoparticles as additive for environmentally stable perovskite solar cells with 20.46% efficiency. *Nano Energy*, 59, pp.517–526.

[95] Tong, G. et al., 2019. Phase transition induced recrystallization and low surface potential barrier leading to 10.91%-efficient $CsPbBr_3$ perovskite solar cells. *Nano Energy*, 65, p.104015.

[96] Wang, R. et al., 2019. A review of perovskites solar cell stability. *Advanced Functional Materials*, 29(47), p.1808843.

[97] Zhao, X. & Park, N.G., 2015. Stability issues on perovskite solar cells. *Photonics*, 2(4), pp.1139–1151.

[98] Zhang, P. et al., 2018. Perovskite solar cells with ZnO electron-transporting materials. *Advanced Materials*, 30(3), p.1703737.

[99] Bella, F. et al., 2016. Improving efficiency and stability of perovskite solar cells with photocurable fluoropolymers. *Science*, 354(6309), pp.203–206.

[100] Arora, N. et al., 2019. Low-cost and highly efficient carbon-based perovskite solar cells exhibiting excellent long-term operational and UV stability. *Small*, 15(49), p.1904746.

[101] Leijtens, T. et al., 2013. Overcoming ultraviolet light instability of sensitized TiO_2 with meso-superstructured organometal tri-halide perovskite solar cells. *Nature Communications*, 4, p.2885.

[102] Sanchez, R.S. & Mas-Marza, E., 2016. Light-induced effects on Spiro-OMeTAD films and hybrid lead halide perovskite solar cells. *Solar Energy Materials and Solar Cells*, 158(2), pp.189–194.

[103] Wei, D. et al., 2016. Photo-induced degradation of lead halide perovskite solar cells caused by the hole transport layer/metal electrode interface. *Journal of Materials Chemistry A*, 4(5), pp.1991–1998.

[104] Xing, M. et al., 2021. Study on the performance of ZMO/PbS quantum dot heterojunction solar cells. *Solar Energy*, 213, pp.53–58.

[105] Aharon, S. et al., 2015. Temperature dependence of hole conductor free formamidinium lead iodide perovskite based solar cells. *Journal of Materials Chemistry A*, 3(17), pp.9171–9178.

[106] Zheng, X. et al., 2016. The controlling mechanism for potential loss in $CH_3NH_3PbBr_3$ hybrid solar cells. *ACS Energy Letters*, 1(2), pp.424–430.

[107] Lin, L. & Ravindra, N.M., 2020. Temperature dependence of CIGS and perovskite solar cell performance: An overview. *SN Applied Sciences*, 2(8), p.1361.

[108] Laamari, M.E. et al., 2019. Optimized opto-electronic and mechanical properties of orthorhombic methylamunium lead halides ($MAPbX_3$) (x = I, Br and Cl) for photovoltaic applications. *Solar Energy*, 182, pp.9–15.

[109] Tumen-Ulzii, G. et al., 2020. Understanding the degradation of Spiro-OMeTAD-based perovskite solar cells at high temperature. *Solar RRL*, 4(10), p.2000305.

[110] Jung, M. et al., 2016. Thermal stability of Cuscn Hole conductor-based perovskite solar cells. *ChemSusChem*, 9(18), pp.2592–2596.

[111] Liu, J. et al., 2019. Growing high-quality $CsPbBr_3$ by using porous $CsPb_2Br_5$ as an intermediate: A promising light absorber in carbon-based perovskite solar cells. *Sustainable Energy & Fuels*, 3(1), pp.184–194.

[112] Domanski, K. et al., 2016. Not all that glitters is gold: Metal-migration-induced degradation in perovskite solar cells. *ACS Nano*, 10(6), pp.6306–6314.

[113] Lee, J. et al., 2020. Graphene interfacial diffusion barrier between CuSCN and Au layers for stable perovskite solar cells. *Carbon*, 157, pp.731–740.

[114] Wu, M. & Ma, T., 2012. Platinum-free catalysts as counter electrodes in dye-sensitized solar cells. *ChemSusChem*, 5(8), pp.1343–1357.

[115] Zhang, H. et al., 2018. Self-adhesive macroporous carbon electrodes for efficient and stable perovskite solar cells. *Advanced Functional Materials*, 28(39), p.1802985.

[116] Valastro, S. et al., 2020. Improved Electrical and structural stability in HTL-free perovskite solar cells by vacuum curing treatment. *Energies*, 13(15), p.3953.

[117] Sigma-Aldrich, *Copper(I) thiocyanate | 99% | 1111-67-7*.

Available at: https://www.sigmaaldrich.com/CA/en/product/aldrich/298212 [Accessed November 22, 2021].

[118] Sigma-Aldrich, *Spiro-MeOTAD | 99% HPLC | 207739-72-8*.

Available at: https://www.sigmaaldrich.com/CA/en/product/aldrich/792071?context=product [Accessed November 22, 2021].